Performance of reanalysis and mesoscale models ~~for wind resource assessment~~ off the coast of ~~Hawaii~~Hawai’i

Lindsay M. Sheridan[1], Raghavendra Krishnamurthy[1], Tien Manh Nguyen[2], Yi-Leng Chen[2], William I. Gustafson Jr.[1], Ye Liu[1], Feng Hsiao[2], Rob K. Newsom[1], Preston Spicer[1], Evgueni Kassianov[1], Mikhail Pekour[1], Nicola Bodini[3], and Mark Severy[1]

[1]Pacific Northwest National Laboratory, Richland, Washington, United States
[2]University of ~~Hawaii~~Hawai’i, Honolulu, ~~Hawaii~~Hawai’i, United States
[3]National Renewable Energy Laboratory, Golden, Colorado, United States

Correspondence to: Lindsay M. Sheridan (lindsay.sheridan@pnnl.gov)

Abstract. The eastern ~~Hawaii~~Hawai’i coast in the United States is characterized by considerable wind resource fuelled by persistent trade winds, making it an important area for ~~wind~~ energy research. The need is strong for reanalyses and~~,~~ higher-resolution regional simulations~~, and purpose-built wind datasets in locations~~ where observations have been historically limited, such as ~~Hawaii~~Hawai’i’s offshore environments. However, studies using offshore observations in other parts of the world have shown that significant errors can occur in reanalyses and wind datasets, which can lead to inaccurate estimates of wind energy generation, payback periods, and extreme weather risks at project locations. The degree of such errors is influenced by a number of factors, including spatial resolution and the handling of processes within the planetary boundary layer (PBL). In this work, we provide a wind resource characterization from year-long lidar buoy measurements off the eastern coast of ~~Oahu~~O’ahu, ~~Hawaii~~Hawai’i, an environment previously unobserved at the rotor level, and use it to establish the performance of two~~four~~ simulation datasets~~ with distinct spatial resolutions and PBL representations~~. The ~~Oahu~~O’ahu deployment location is meteorologically unique and less complex~~ compared with previous offshore wind performance study locations~~, being strongly characterized by the trade winds with minimal land-atmosphere interaction influences. Despite the unique and consistent conditions, we hypothesize that distinct simulation datasets will exhibit diverse ranges of errors similar to what has been seen for other offshore locations. We find the European Centre for Medium-Range Weather Forecasts (ECMWF) Reanalysis version 5 (ERA5) to strongly underestimate observed wind speeds at the ~~Oahu~~O’ahu location (bias = -1.54~~3~~ m s^{-1} at a ~~hub~~ height of 140 m above sea level), while a regional Weather Research and Forecasting (WRF) Model simulation produced by the University of ~~Hawaii~~Hawai’i (UH-WRF) provides a significantly smaller wind speed bias (-0.25 m s^{-1}), highlighting the value of running regional, higher-resolution simulations. ~~Despite not temporally overlapping with the Oahu deployment, the long-term annual average 140 m wind speeds from the 2023 National Offshore Wind dataset (NOW-23) and Global Wind Atlas version 3 (GWA3) produce smaller magnitude biases (+0.39 m s^{-1} and -0.10 m s^{-1}, respectively) than ERA5.~~ The large bias noted for ERA5 is driven by significant underestimation of fast wind speeds (> 9 m s^{-1}), which the study site is largely characterized by, along with discontinuities in the ERA5 diurnal cycle. We also speculate that the

relative sparsity of observations for data assimilation in this remote part of the world could influence the performance of ERA5 and that challenges with characterizing island effects could impact the performance of both datasets.

1 Introduction

Simulated wind data, including long-term reanalysis models and higher-resolution wind datasets, are essential for assessing the ~~offshore~~ wind resource near ~~Hawaii~~Hawai'i and locations around the world due to the scarcity of wind observational coverage over the water. Many recent studies have assessed offshore wind energy potential using reanalysis models, in particular, ERA5 (Hersbach et al., 2020) and the Modern-Era Retrospective analysis for Research and Applications version 2 (MERRA-2) (Gelaro et al., 2017), given their advantageous temporal and geographical coverages and their ease of data accessibility versus observational campaigns in challenging marine environments (Soares et al., 2020; Hayes et al., 2021; Nehzad et al., 2021; Soukissian et al., 2021; Cowin et al., 2023). At locations where offshore hub height wind measurements do exist, wind researchers can follow the methodology of the land-based wind industry in using measure-correlate-predict techniques, which are extensively reviewed by Carta et al. (2013), to extend the temporal coverage of the observations with reference reanalysis data. Reanalysis models also serve as the forcings for higher-resolution datasets developed to serve the wind energy community, such as Global Wind Atlas ~~version 3 (GWA3)~~ (Davis et al., 2023) and the 2023 National Offshore Wind dataset (NOW-23) (Bodini et al., 2024a).

Despite the wide applicability and need for simulated wind datasets, such products contain inaccuracies with respect to observations that can lead to significant errors in parameters relevant to wind energy researchers and developers, such as the annual and long-term average wind speed, seasonal and diurnal trends in wind speed, and occurrences of weather-driven events like wind ramps. Therefore, assessing and disseminating the performance of simulated datasets in previously unstudied locations is necessary for understanding the risks of wind resource estimation and enabling the adjustment of estimates as a means of improving accuracy. Due to the difficulty of collecting wind measurements over open water, validations of reanalysis models and wind resource datasets are limited for offshore environments, particularly at heights relevant to offshore wind turbine rotor layers, which on average covered heights between 32 m and 216 m for turbines installed globally in 2023 (McCoy et al., 2024). However, floating lidar technology and tall meteorological towers deployed on offshore platforms have increased opportunities to validate models and datasets in areas of ~~offshore wind development interest~~deep water energy developments.

With the increasing availability (though still a relatively small sample) of offshore rotor level observations, studies have emerged over recent years comparing the performance of multiple simulation datasets at turbine rotor heights in offshore locations with the aims of aiding analysts in selecting the optimal datasets for resource assessments and highlighting areas for accuracy improvement for dataset developers. These studies have shown significant differences in performance across simulations being validated at a single offshore location, and in some cases one simulation product can be the best performer for one error metric (bias, correlation, mean absolute error, etc) and the worst performer for another metric. A variety of wind performance studies have evaluated ERA5 and note that the reanalysis tends to underestimate observed wind speeds (Kalverla et al., 2020 over the North Sea; Sheridan et al., 2020 off the eastern coast of the United States; Pronk et al., 2022 and Fragano and Colle, 2025 off the eastern coast of the United States; Sheridan et al., 2022 off the western coast of the United States). Several offshore studies find that higher-resolution datasets improve upon ERA5 in terms of wind speed bias (Kalverla et al., 2020 examining the Dutch Offshore Wind Atlas; Pronk et al., 2020 examining the Wind Integration National Dataset Toolkit Long-term Ensemble Dataset (WTK-LED); Fragano and Colle, 2025 examining NOW-23) but note that ERA5 outperforms the higher-resolution datasets according to other error metrics or wind field characteristics.

~~For observed wind profiles over the North Sea, Kalverla et al. (2020) found the Dutch Offshore Wind Atlas to have near zero bias, while ERA5 underestimated the observed wind speed by approximately 0.5 $\mathrm{m\ s^{-1}}$ regardless of height. At lidar buoy deployment sites off the coasts of Virginia and New Jersey, United States, Sheridan et al. (2020) noted that ERA5, MERRA-2, the Rapid Refresh (RAP) analysis, and the North American Regional Reanalysis tended to underestimate observed wind speeds, with MERRA-2 providing the smallest magnitude biases and RAP producing the largest magnitude biases at both sites when using a dynamic power law to adjust the model heights to the lidar height of 90 m. From a different lidar buoy off the coast of New Jersey, United States, Pronk et al. (2022) determined that ERA5 yielded a significant negative wind speed bias (around -1 $\mathrm{m\ s^{-1}}$), while the higher-resolution Wind Integration National Dataset Toolkit Long-term Ensemble Dataset (WTK-LED) had a reduced bias near -0.5 $\mathrm{m\ s^{-1}}$. However, Pronk et al. (2022) found that ERA5 outperformed WTK-LED in terms of centered root-mean-square error (CRMSE) at the same site. Using observations from the same floating lidar as Pronk et al. (2022), Fragano and Colle (2025) established that NOW-23 significantly outperforms ERA5 in terms of wind speed bias, especially during the spring when they found biases ranging from -0.35 $\mathrm{m\ s^{-1}}$ at 40 m to -0.90 $\mathrm{m\ s^{-1}}$ at 140 m for ERA5 and +0.25 $\mathrm{m\ s^{-1}}$ at 40 m to -0.30 $\mathrm{m\ s^{-1}}$ at 200 m for the regional offshore wind dataset NOW-23. Despite NOW-23 showing significantly lower wind speed biases than ERA5 off the coast of New Jersey, Fragano and Colle (2025) found that NOW-23 had notably larger wind speed mean absolute errors than ERA5 in all seasons except spring. Based on lidar buoy data off the California, United States coast, Sheridan et al. (2022) validated five models and found that MERRA-2 produced the smallest wind speed bias (near zero) at a site off northern California but the largest magnitude bias (-1.6 $\mathrm{m\ s^{-1}}$) at a site off central California, while RAP provided the highest correlations for both sites (0.88 and 0.94).~~

Variations across wind simulations for performance metrics like bias and correlation occur for a number of reasons. In their evaluation of reanalysis products, Ramon et al. (2019) found that the lowest correlations for wind speeds compared with global tall tower observations corresponded to the coarsest resolution grids. Similarly, Kalverla et al. (2020) attributed ERA5's horizontal resolution to underestimation of observed offshore wind ramps due to limitations in the model representation of the small-scale structures responsible for ramps. Sheridan et al. (2022) noted that the high correlation of the Rapid Refresh model~~RAP~~ with offshore California observations was at least partly due to the model's higher resolution and therefore better ability at resolving coastal features and phenomena that coarser models miss. Pronk et al. (2022) determined that the preliminary WRF simulations for WTK-LED outperformed ERA5 in terms of bias at an onshore site and an offshore site in the United States but found the opposite behaviour~~trend~~ for centred root-mean-square error (CRMSE). Pronk et al. (2022) suspected that the underperformance of WTK-LED for CRMSE is due to WTK-LED's exaggeration of the diurnal cycle of wind speeds at both study sites, especially the onshore location. Bodini et al. (2024b) tested two PBL schemes in simulations off the coast of California using lidar buoy observations and established that using the Mellor-Yamada-Nakanishi-Niino (MYNN) scheme overestimated stability compared with observations and simulations using the Yonsei University (YSU) scheme~~-based simulations~~, resulting in overestimation of offshore~~ hub height~~ wind speeds~~ in the region using MYNN~~ and the selection of YSU as the PBL scheme for the NOW-23 South Pacific region. ~~Nunalee and Basu (2014) tested six PBL schemes within WRF to replicate low-level jet (LLJ) events off the United States Northeastern Seaboard, which are impactful on the available wind resource for turbine production, and found that all of them underestimated jet core intensity and struggled to represent a weak LLJ but accurately simulated the timing and termination of jet development and termination. Nunalee and Basu (2014) noted inconsistencies among the PBL schemes for replicating LLJs, such as the Mellor-Yamada-Janjic and Quasi Normal Scale Elimination parameterizations performing the worst and subsequently the best for two LLJ events separated by 1.5 days.~~

To address the need for wind resource characterization and model validation in offshore environments, the U.S. Department of Energy (DOE) has collaborated with the Bureau of Ocean Energy Management (BOEM) to deploy multiple buoy-mounted research lidars in locations that had~~itherto have~~ not previously been observ~~explor~~ed ~~in an observational manner~~ at relevant ~~turbine~~ heights for deep water energy development. In late 2022, one of the lidar buoys was deployed off the eastern shore of ~~Oahu~~O'ahu to gather meteorological and oceanographic~~ocean~~ observations ~~in support of future offshore wind development~~(Appendix A). ~~While the first offshore wind call areas in Hawaii were located northwest and southwest of Oahu (McCoy et al., 2024), the eastern side of the island has optimal exposure to the northeast trade winds that dominate the region and the deployment offers the first observation-based understanding of the rotor-level wind resource in the area.~~ The ~~Oahu~~O'ahu lidar buoy deployment lasted a period of one year, which captured a full seasonal cycle of marine boundary layer~~offshore wind~~ observations. In addition to the onboard lidar, the buoy was equipped with a suite of surface meteorological and oceanic instruments to produce a more complete analysis of atmospheric and oceanic~~ metocean~~ impacts on the wind resource.

With the knowledge in mind that no simulated dataset will perfectly replicate wind observations, we conjecture that some datasets will perform better than others in representing the wind resource at the previously unstudied buoy deployment location off ~~Oahu~~O'ahu, leading to recommended use cases of these products for analysts in the wind energy community. ~~In particular, we hypothesize that ERA5 will exhibit a low wind speed bias at our study site akin to previous offshore evaluations and that higher-resolution datasets will find greater success at representing the observations.~~ While many of the previous ~~offshore~~ wind validations have occurred in marine locations regularly influenced by nearby land-atmosphere interactions, like sea breezes and low-level jets, this study presents a unique look into model performance at the rotor level in a trade wind dominant environment. Our analysis evaluates the successes and challenges of two~~four~~ diverse datasets~~, ranging from a geographically coarse reanalysis product (ERA5) to a high-resolution climatology dataset (GWA3),~~ in representing the observed winds from the ~~Hawaii~~Hawai’i lidar buoy deployment. To set the stage for the validation, we begin in Section 2 with a discussion of the observed meteorological findings from the lidar buoy and then describe each wind dataset and the methods for evaluation. Section 3 provides the assessment of~~ the~~ two datasets that temporally overlap with the lidar buoy deployment: the reanalysis ERA5 and a regional WRF simulation produced by the University of ~~Hawaii~~Hawai’i, UH-WRF. Due to the concurrency of the observations and estimates, this section goes into detail on the dataset performance according to factors like wind shear~~stability~~, wind speed class, and various meteorological phenomena that occurred during the deployment. ~~Section 4 explores the similarities and differences between the lidar buoy observations and the two datasets that are not concurrent: NOW-23 and GWA3. We keep this evaluation a high-level comparison to determine whether the observed wind speeds and trends are represented in the ranges of simulated long-term wind speeds, as we acknowledge that the significant limitation of temporally misaligned datasets does not allow for a comprehensive validation.~~ Finally, Section 4 synthesizes the results from the wind speed evaluations to assess their implications for modelling atmospheric dynamics and boundary layer processes. The section concludes with insights into improving model accuracy and representation of complex atmospheric phenomena, offering guidance for refining simulation techniques and observational strategies in unstudied regions.~~Finally, Section 5 ties the results from the wind speed evaluations to impacts on wind energy estimation and concludes with recommendations for improving offshore wind resource assessment based on this and other analyses.~~ The manuscript also provides Appendix A, which reports on the recovery, quality, and processing of the data from the ~~Hawaii~~Hawai’i deployment.

2 Data and methodology

To set the stage for assessing the performance of reanalysis and mesoscale models using lidar buoy observations in a new offshore location, the next sections present an overview of the buoy observations, a brief characterization of the local wind resource, descriptions of the models that will be validated, and the procedure for establishing model performance success.

Formatted: Normal

~~DOE owns multiple AXYS WindSentinel™ buoys, including the buoy deployed for resource assessment off the coast of Oahu which is outfitted with a Leosphere Windcube v2 lidar system and surface meteorological and oceanographic instruments (Figure 1). Prior to deployment off of Oahu, the lidar buoy underwent validation at Woods Hole Oceanographic Institution’s Martha’s Vineyard Coastal Observatory from January to June 2020 and was subsequently deployed off the Humboldt County, California coast from October 2020 to December 2021. The validation at Martha’s Vineyard utilised an International Electrotechnical Commission-certified reference lidar atop an offshore platform approximately 250 m from the lidar buoy. The validation produced wind speed coefficients of determination (R^2) exceeding 0.98 and wind direction R^2 values exceeding 0.97 up to 200 m above sea level (a.s.l.) (Gorton and Shaw, 2020).~~

Field Code Changed

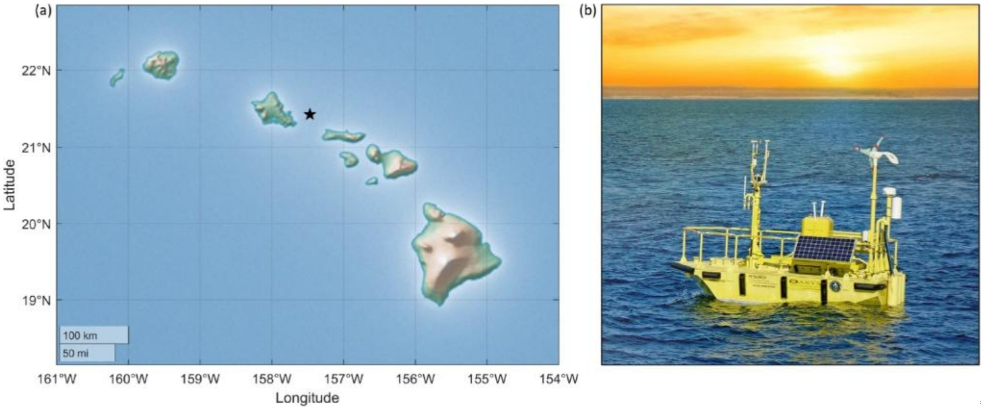

~~**Figure 1.** (a) Map of location of the Hawaii DOE lidar buoy deployment (indicated by the star). (b) Photo of one of the DOE lidar buoys by Ocean Tech Services, LLC and Pacific Northwest National Laboratory.~~

2.1 Buoy observations

DOE owns multiple AXYS WindSentinel^{TM} buoys, including the buoy deployed for resource assessment off the coast of ~~Oahu~~O’ahu which is outfitted with a Leosphere Windcube v2 lidar system and surface meteorological and oceanographic instruments (Figure 1~~Figure 1~~). While the DOE buoy observations during the ~~Hawaii~~Hawai’i deployment are discussed extensively in Appendix A, we provide the key characteristics of the lidar wind measurements to set a baseline for comparison with the wind datasets. Many of the observed characteristics are also found throughout the results to provide context for the evaluations of wind dataset performance. The DOE buoy was deployed approximately 25 km off the coast of ~~Oahu~~O’ahu between 1 December 2022 and 15 December 2023 (DOE, 2025a, b, c) (Figure 1). This study focuses on the~~e lidar aboard the buoy outputs~~ wind data measured by the lidar aboard the buoy at every 20 m between 6~~4~~0 m and 240 m. ~~However, early in the deployment it was noted that the 40 m wind output appeared corrupt, therefore this range gate was adjusted higher in the atmosphere on 12 May 2023 with a new output height of 49 m.~~ Following the quality control performed as discussed in Appendix A, lidar data recovery for the deployment period is 98% or higher for all heights between 60 m and 240 m~~m and greater than 99% for data at 49 m between 12 May 2023 and 15 December 2023~~.

Formatted: Don't keep with next

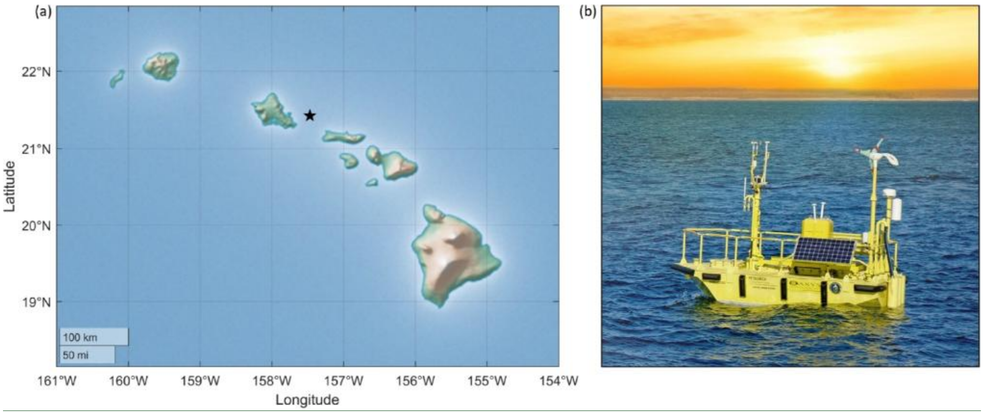

Figure 1. (a) Map of location of the ~~Hawaii~~Hawai’i DOE lidar buoy deployment (indicated by the star). (b) Photo of one of the DOE lidar buoys by Ocean Tech Services, LLC and Pacific Northwest National Laboratory.

Formatted: Caption

2.2 Local wind characterization

For the overlapping period covering the buoy deployment, ERA5, and UH-WRF (1 January – 15 December 2023), annual average wind speeds range from 8.87 m s^{-1} at 60 m to 9.34 m s^{-1} at 240 m with very little shear across the profile (Figure 2a). The observed winds predominantly source from the east-northeast with very little veer across the profile (Figure 2b). The observed 2023 seasonal and diurnal variations in the lidar wind speeds are presented in detail in Section 3.1, but briefly, significant variation is noted for the month-by-month transitions (Figure 2c) while the diurnal wind speed cycle transitions smoothly from hour-to-hour (Figure 2d).

~~For the buoy deployment period, annual average wind speeds range from 8.92 m s^{-1} at 60 m to 9.41 m s^{-1} at 240 m with very little shear across the profile (Figure 2a). The observed winds predominantly source from the east-northeast with very little veer across the profile (Figure 2b). Conversely to seasonal wind patterns determined over a long period of time, which tend to smoothly transition from one month to the next, the average wind speeds during the year-long Hawaii buoy deployment are extremely inconsistent from one month to the next in the winter and fall (Figure 5). Using the 140 m output height as an example based on announced future offshore wind hub heights (McCoy et al., 2024), the monthly average wind speeds for the first four months of the deployment (December 2022 – March 2023) are consecutively 8.60 m s^{-1}, 6.30 m s^{-1}, 11.96 m s^{-1}, and 8.23 m s^{-1}. Following steadier transitions in the monthly average wind speeds throughout the spring and summer, the deployment concludes with another highly oscillatory period between September and November 2023 when the monthly average 140 m wind speeds are consecutively 9.91 m s^{-1}, 5.97 m s^{-1}, and 9.78 m s^{-1}. The standard deviation of the~~

~~140 m monthly average wind speeds over the Hawaii deployment is 1.69 m s^{-1}. Conversely, the observed wind speeds transition steadily across the diurnal cycle, with the fastest wind speeds occurring during the evening and at night and the slowest wind speeds occurring during the day (Figure 6). The standard deviation of the 140 m hourly average wind speeds is 0.27 m s^{-1}.~~

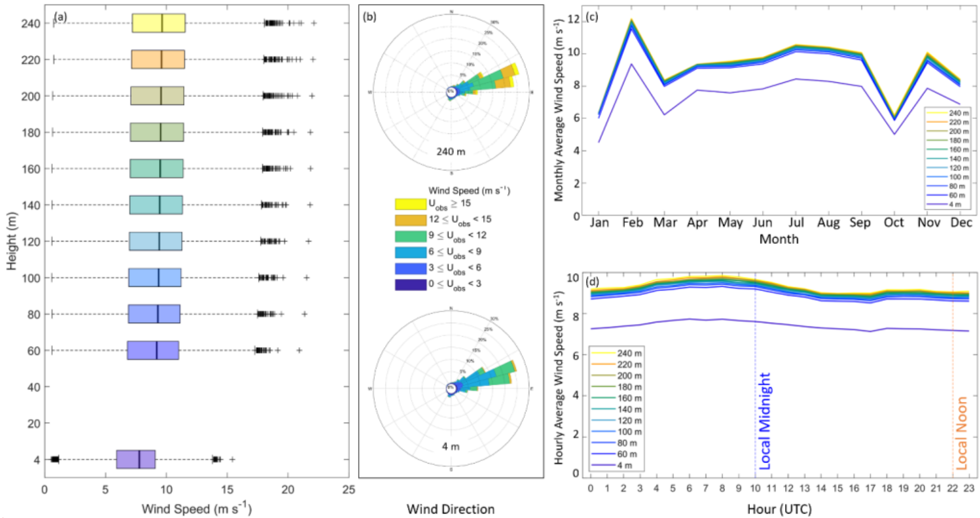

Formatted: Font: Not Bold

Formatted: Caption, Don't keep with next

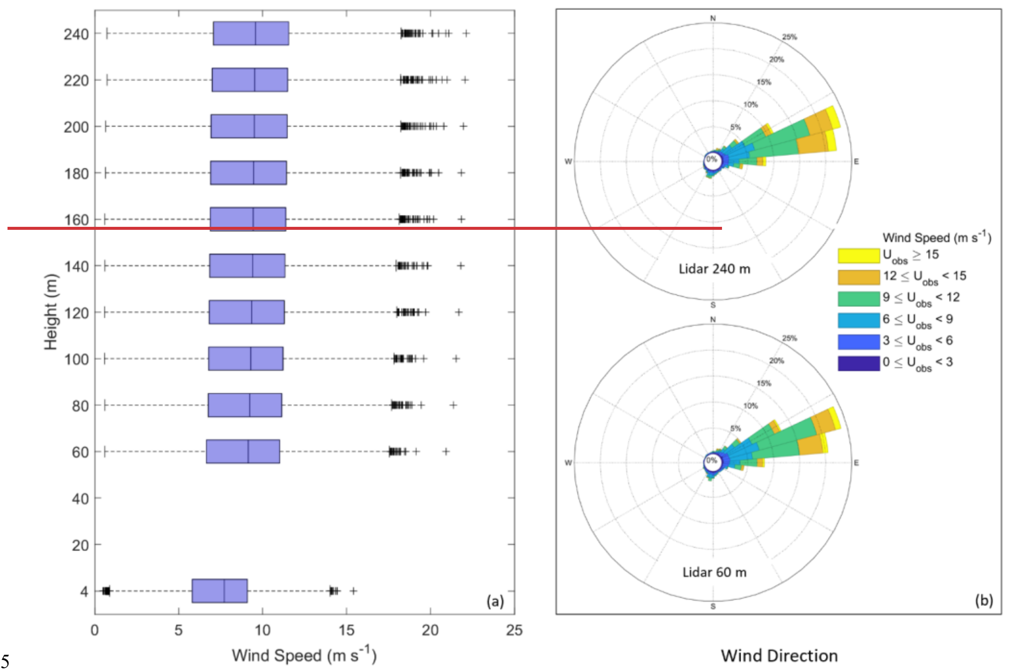

Figure 2. Observed (a) wind speed,~~ and~~ (b) wind direction, (c) monthly average wind speed, and (d) hourly average wind speed by height a.s.l. from the ~~Hawaii~~Hawai'i lidar buoy during 1 January~~December~~ 2023~~2~~ – 15 December 2023. Measurements at 60 m and higher source from the onboard lidar system (DOE, 2025a) while measurements at 4 m source from the onboard surface meteorological station (DOE, 2025b).

Formatted: Font: 9 pt, Not Bold

Formatted: Font: 9 pt, Not Bold

Formatted: Font: 9 pt, Not Bold

Formatted: Font: 9 pt, Not Bold

Formatted: Font: 9 pt, Not Bold

2.2 Models and datasets

Reanalysis models support wind energy analysis in a variety of ways, including providing wind resource assessments and serving as the boundary conditions for higher-resolution modelling efforts. The global geographic coverage and long-term continuously updating temporal coverage of ERA5 allows for widespread use and validation (Table 1~~Table 1~~). ERA5 is developed by ECM~~MC~~WF and the hourly data on the lowest 9 of 137 model levels are used in this study (CDS, 2025a). Data assimilation is performed using a 12-hour 4D-Var ensemble (Hersbach et al., 2020).

The University of ~~Hawaii~~Hawai'i produced a year-long (2023) WRF v4.6.0 simulation (UH-WRF) with the innermost domain covering the islands of Maui, Lanai, ~~Molokai~~Moloka'i, and ~~Oahu~~O'ahu (Table 1~~Table 1~~). The key configurations include the WRF Single-Moment 6-class Microphysics scheme for representing the cloud microphysical processes, the Betts-Miller-Janjic cumulus parameterization for convective processes on the regional domain, the Rapid Radiative Transfer

Model for Global Circulation Models for longwave and shortwave radiation, the Noah land-surface model, and the ~~Yonsei University (~~YSU~~)~~ planetary boundary layer (PBL) scheme (Hsiao et al., 2020, 2021). The lowest 6 of 51 model levels from UH-WRF are evaluated in this study at hourly resolution. UH-WRF was initialized daily using ERA5 data beginning at 0 UTC each day with simulation hours t = 0-35. The land surface data, including terrain, soil type, ground vegetation cover, and soil moisture were updated following the procedures described by Zhang et al. (2005) and Hsiao et al. (2020). The model spin up time occurred between t = 0-11. For this analysis, we build the UH-WRF timeseries using forecast hours t = 12-35.

~~In addition to ERA5 and UH-WRF, which provide wind information along with a variety of other earth and atmospheric variables, specific datasets have been developed for wind energy research and development. NOW-23, developed by the National Renewable Energy Laboratory (NREL), the University of Colorado, and Veer Renewables to support offshore wind research, consists of eight regional WRF model simulations: three for the Atlantic Ocean, two for the Pacific Ocean, one for the Great Lakes, one for the Gulf region, and one for Hawaii (Bodini et al., 2024a). The model parameters are custom to each regional simulation to account for geographically unique wind resource phenomena. The NOW-23 Hawaii simulation uses ERA5 to provide the boundary conditions, the Mellor-Yamada-Nakanishi-Niino (MYNN) scheme for the PBL and surface layer schemes, the Noah land-surface model, and the Operational Sea Surface Temperature and Ice Analysis (OSTIA) for the sea surface temperature (Bodini et al., 2024a). Wind data are output at 18 heights between 10 m and 500 m at 5-min resolution (Table 1). Wind analysts can access NOW-23 and other wind datasets through the Wind Resource Database (NREL, 2025).~~

~~GWA3, developed by the Technical University of Denmark (DTU) and World Bank Group, utilises the WRF model with the Mellor-Yamada-Janjić (MYJ) PBL scheme and ERA5 as input and boundary conditions to produce simulated wind data with a 3-km horizontal resolution (Davis et al., 2023). From there, microscale modelling using the Wind Atlas Analysis and Application Program (WAsP) model is performed to achieve an output grid spacing of 250 m. GWA3 provides global coverage for land-based wind estimates and offshore wind estimates within 200 km of shorelines. Wind data are output at five heights between 10 m and 200 m at annual, monthly, and diurnal temporal resolutions (Table 1). Users can access GWA3 through its web application (DTU, 2025).~~

Table 1. Characteristics of wind assessment products evaluated in this analysis.

Product	**ERA5**	**UH-WRF**
Type	Reanalysis	Meteorological dataset
Developers	ECMWF	University of ~~Hawaii~~Hawai'i
Temporal coverage	1950 – present	2023
Temporal resolution	1-hr	1-hr
Spatial coverage	Global	~~Hawaii~~Hawai'i
Horizontal s~~S~~patial resolution	31-km	1.5-km

Formatted Table

PBL handling	First-order K-diffusion closure of Monin-Obukhov similarity theory in the surface layer and above the surface layer, except for unstable conditions when scheme is an eddy-diffusivity mass flux framework (Fragano and Colle, 2025) plus effects of d~~D~~ata assimilation	YSU scheme
Wind output heights used in this study	Lowest 9 (of 137) model heights: 4 m, 26 m, 50 m, 76 m, 105 m, 136 m, 171 m, 208 m, 249 m at the buoy location	Lowest 6 (of 51) model heights: 0 m, 51 m, 85 m, 145 m, 187 m, 256 m at the buoy location

[a] ~~Depending on the region, the temporal extent varies between 2019 and 2022. For Hawaii, the temporal extent of NOW-23 is 2019.~~

Formatted: Font: (Default) +Body (Times New Roman), 8 pt

2.3 Validation methodology

To assess the performance of~~For the two models that temporally overlap with the Hawaii buoy deployment,~~ ERA5 and UH-WRF in representing the observed wind speeds from the lidar buoy, the bias~~ (Eq. 1)~~, correlation~~ (Eq. 2)~~, and CRMSE~~ (Eq. 3)~~ are determined for the N timestamps that the observed wind speeds (U_{obs}) and simulated wind speeds (U_{sim}) from both datasets are available, to ensure a consistent comparison. ~~The variables $\overline{U_{obs}}$ and $\overline{U_{sim}}$ are the average observed and simulated wind speeds, respectively, over the period N.~~ The wind speed bias provides a gauge of whether the models tend to overestimate (positive bias), underestimate (negative bias), or accurately represent (zero bias) the observed wind speeds. The Pearson correlation coefficient explains the degree to which the simulated and observed wind speeds are linearly related, with values near 1 indicative of a high degree of correlation. The CRMSE portrays the degree of variation in error between the simulated and observed wind speeds, with larger values indicating larger errors.

$$bias = \frac{1}{N}\sum_{i=1}^{N}\left(U_{sim,i} - U_{obs,i}\right) \quad \text{(1)}$$

$$correlation = \frac{\sum_{i=1}^{N}\left(U_{sim,i} - \overline{U_{sim}}\right)\left(U_{obs,i} - \overline{U_{obs}}\right)}{\sqrt{\sum_{i=1}^{N}\left(U_{sim,i} - \overline{U_{sim}}\right)^{2}}\sqrt{\sum_{i=1}^{N}\left(U_{obs,i} - \overline{U_{obs}}\right)^{2}}} \quad \text{(2)}$$

$$CRMSE = \sqrt{\frac{1}{N}\sum_{i=1}^{N}\left(\left(U_{sim,i} - \overline{U_{sim}}\right) - \left(U_{obs,i} - \overline{U_{obs}}\right)\right)^{2}} \quad \text{(3)}$$

~~Analysis of the performance of NOW-23 and GWA3 off the coast of Oahu is significantly limited by the temporal misalignment between the dataset coverage periods (2000 – 2019 and 2008 – 2017, respectively) and the lidar buoy observation period (1 December 2022 – 15 December 2023). Therefore, we utilise the entire temporal coverage periods of~~

~~NOW-23 and GWA3 to establish whether the observed wind speeds and the observed seasonal and diurnal wind speed trends are represented in the ranges of the simulated long-term wind speeds.~~In order to explore the performance of ERA5 and UH-WRF in representing key characteristics of the marine atmospheric boundary layer at the location of the Hawai'i lidar buoy deployment, the simulation datasets must be spatially aligned with the measurements. Vertically, the model level wind speeds are adjusted to the observed near surface (4 m) and lidar output heights (every 20 m between 60 m and 240 m), z, using the power law (Eq. 2) with the wind shear exponent α (Eq. 1) calculated at every timestamp using the surrounding model heights z_{lo} and z_{hi} and the associated wind speeds u_{lo} and u_{hi}. The performance analysis of ERA5 and UH-WRF considers the entire wind profile up to 240 m (the limit of the lidar observations) along with a focused investigation at a single height, 140 m a.s.l. The wind datasets selected for evaluation range widely in terms of horizontal spatial resolution, from 1.5-km (UH-WRF) to approximately 27-km at the location of the buoy deployment (ERA5) (Table 1). For each dataset, we perform inverse distance weighting on the atmospheric variables to localize them to the location of the lidar buoy. For reference, the nearest grid points to the buoy location are at distances of 0.9 km (UH-WRF) and 10 km (ERA5). The four surrounding UH-WRF grid points to the buoy are at distances of 21-24 km from the nearest coastline (O'ahu). The four surrounding ERA5 grid points to the buoy are at distances of 3 km (Moloka'i), 17 km (O'ahu), 24 km (O'ahu), and 31 km (Moloka'i) from the nearest coastline.

$$\alpha = \frac{\ln(u_{hi}/u_{lo})}{\ln(z_{hi}/z_{lo})} \tag{1}$$

$$u = u_{lo}\left(\frac{z}{z_{lo}}\right)^{\alpha} \tag{2}$$

Formatted: Font: Italic

Formatted: Font: Italic

Formatted: Font: Italic

Formatted: Font: Italic

3 Year-long model validation

~~The following studies compare the performance of ERA5 and UH-WRF in representing key characteristics of the offshore wind resource at the location of the Hawaii lidar buoy deployment. For ERA5 and UH-WRF, the model level wind speeds are adjusted to the observed near surface (4 m) and lidar output heights (every 20 m between 60 m and 240 m) z using the power law (Eq. 5) with the wind shear exponent α (Eq. 4) calculated at every timestamp using the surrounding model heights~~ ~~z_{lo} and z_{hi} and the associated wind speeds u_{lo} and u_{hi}. The performance analysis of ERA5 and UH-WRF considers the entire wind profile up to 240 m (the limit of the lidar observations) along with a focused investigation at a single height, 140 m a.s.l., based on the announced hub heights for upcoming offshore wind projects (McCoy et al., 2024). Comparisons are performed using only hours when both the buoy observations and model estimates are available.~~

~~$\alpha =$~~ ~~(4)~~

~~$u =$~~ ~~(5)~~

Prior to comparing the O’ahu observations, which predominantly occur in the year 2023, with atmospheric datasets, it is imperative to provide context on what kind of meteorological year 2023 is relative to the long-term interannual wind speed variability noted at the deployment location. Utilising annual averages of the Oceanic Niño Index (ONI), we find that 2023 is categorized as an El Niño year based on the Climate Prediction Center’s threshold of +/- 0.5°C (Figure 3a) (NOAA, 2025). In Figure 3b, we explore the annual average ERA5 100 m wind speeds (CDS, 2025b) between 1985 and 2024 and determine that 2022 and 2023 are tied for having the lowest annual average wind speeds over the 40-year period (annual average wind speeds normalized by the 40-year mean for both years = 0.88) while being opposingly classified as La Niña and El Niño years, respectively (Figure 3a). According to ERA5, precipitation and 2 m temperature are above average at the buoy location for the year 2023 (Figure 3c, d). The above average precipitation, temperature, and weakening of the trade winds are consistent with expected El Niño characteristics (Lu et al., 2020).

The following analyses focus on the performance of two simulation datasets that have concurrent temporal coverage with the 2023 observations: ERA5 and UH-WRF. Given the context of 2023 being a record low wind resource year east of O’ahu according to the ERA5 record, it is important to note the need for long-term, continuously updating datasets like reanalyses. Purpose-built wind datasets, like NOW-23 (2000-2019) and Global Wind Atlas (2008-2017), provide numerous years for wind resource assessment but would not represent the characteristics of an atypical year like 2023.

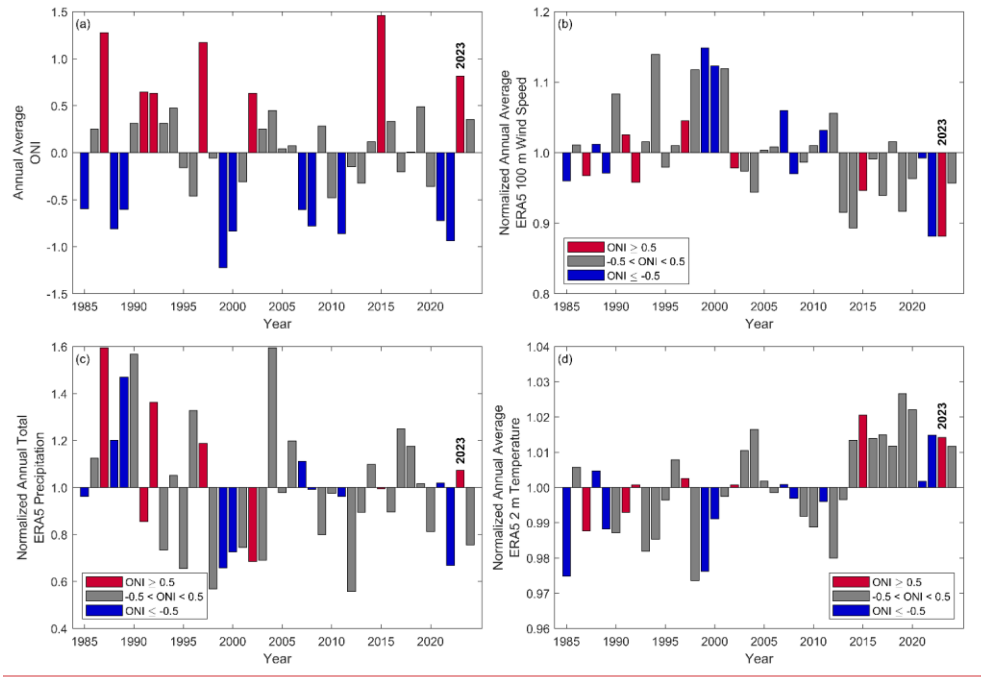

Figure 3. (a) Annual average ONI, (b) normalized annual average 100 m wind speed from ERA5, (c) normalized annual total precipitation from ERA5, and (d) normalized annual average 2 m temperature from ERA5 over the 40-year period between 1985 and 2024 coloured by the annual average ONI. The annual average wind speeds are normalized by the 40-year average wind speed at the O'ahu buoy deployment location.

Formatted: Caption

3.1 Annual, seasonal, and diurnal performance

During the nearly year-long overlapping period of the buoy deployment, UH-WRF, and ERA5 (1 January 2023 – 15 December 2023)~~ period~~, ERA5 strongly underestimates the observed wind speeds across the profile with~~ average~~ biases ranging from -1.52~~3~~ m s^{-1} to -1.54~~62~~ m s^{-1} (-1.54~~3~~ m s^{-1} at 140 m) (Figure 4). UH-WRF underestimates the observed wind speeds across the profile as well, but to a lesser degree, with~~ average~~ biases ranging from -0.24 m s^{-1} to -0.29 m s^{-1} (-0.25 m s^{-1} at 140 m) (Figure 4). The correlations for both ERA5 (0.88~~9~~-0.89~~90~~) and UH-WRF (0.84-0.85) suggest successful representation of the hourly fluctuations in the observed wind speeds (Figure 4~~Figure 3~~a). Previous DOE lidar buoy deployments off the northern and central coasts of California revealed similar correlations for ERA5 (0.88) (Sheridan et al., 2022). The CRMSEs during the ~~Hawaii~~Hawai'i buoy deployment (ERA5 = 1.59~~8~~-1.62~~60~~ m s^{-1}, UH-WRF = 1.96-2.02 m s^{-1})

(Figure 4~~Figure 3~~a) are notably lower than the ERA5-based CRMSEs found during the California deployments, which ranged between 2.3 m s^{-1} and 2.4 m s^{-1}.

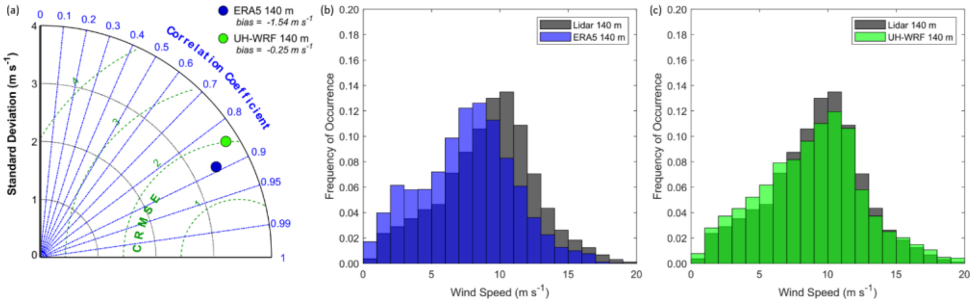

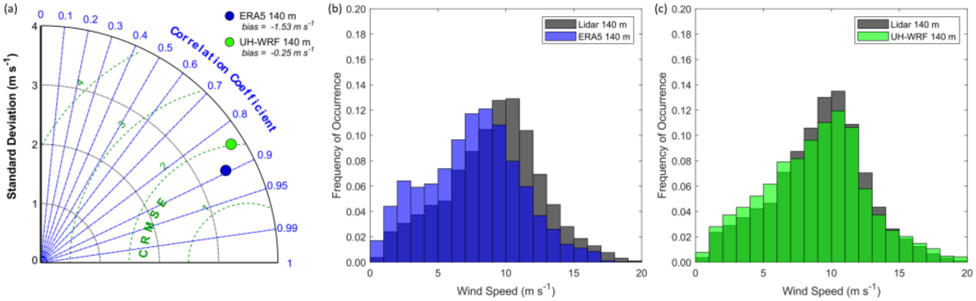

Figure 4~~3~~. ERA5~~ (140 m, 1 December 2022 – 15 December 2023)~~ and UH-WRF~~ (140 m, 1 January 2023 – 15 December 2023)~~ wind speed (a) correlations, standard deviations, and CRMSEs, and (b), (c)~~, (d)~~ distributions at the ~~Hawaii~~Hawai'i buoy location during the overlapping period of 1 January 2023 – 15 December 2023.

The model wind speed biases during the ~~Hawaii~~Hawai'i buoy deployment differ significantly depending on the magnitude of the observed wind speed. We use the NREL 15 MW~~ offshore~~ wind reference power curve (Musial et al., 2019) to categorize the observed 140 m wind speeds according to pre-cut-in wind speeds (≤ 3 m s^{-1}), wind speeds along the steep portion of the power curve (> 3 m s^{-1} and < 11 m s^{-1}), and wind speeds corresponding to maximum power production (≥ 11 m s^{-1}). During the full-year deployment period, 6~~5.8~~%, 65~~.2~~%, and 29~~.0~~% of the lidar 140 m wind speeds fall into the pre-cut-in, steep portion, and maximum power categories, respectively. No observed or modelled 10-minute averaged wind speeds at any height between the surface and 240 m a.s.l. during the ~~Hawaii~~Hawai'i buoy deployment exceeded the cut-out wind speed denoted by the reference power curve (25 m s^{-1}), so biases during wind speed cut-out or derate periods are not able to be determined.

ERA5 and UH-WRF follow similar pattern~~trend~~s in bias according to the observed wind speed (Figure 5~~Figure 4~~). In representing the observed pre-cut-in wind speeds at 140 m, ERA5 exhibits little bias (median = 0.15~~09~~ m s^{-1}) while UH-

WRF significantly overestimates (median bias = 0.83 m s^{-1}). For observed wind speeds on the steep portion of the power curve, ERA5 and UH-WRF underestimate with median biases of -1.349 m s^{-1} and -0.25 m s^{-1}. The greatest ERA5 errors are determined for observed wind speeds corresponding to maximum turbine generation, at the top of the power curve. For these faster observed wind speeds, ERA5 displays significant underestimation, with a median bias of -1.74~~1~~ m s^{-1}, while UH-WRF produces a median bias of -0.30 m s^{-1}.

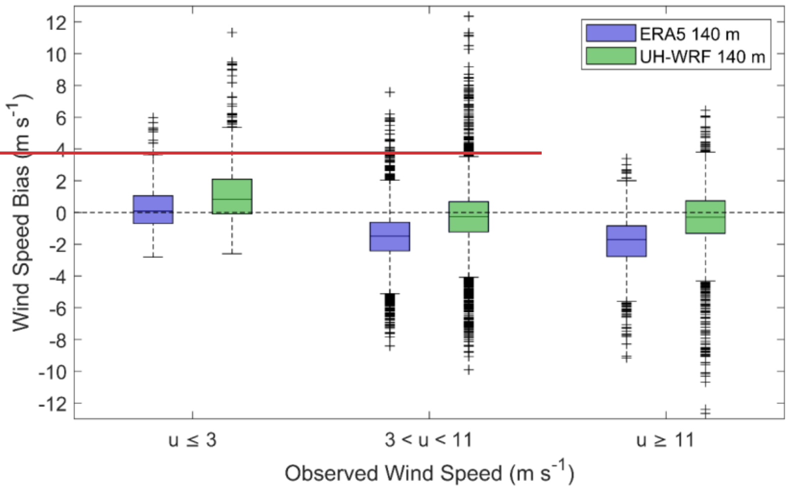

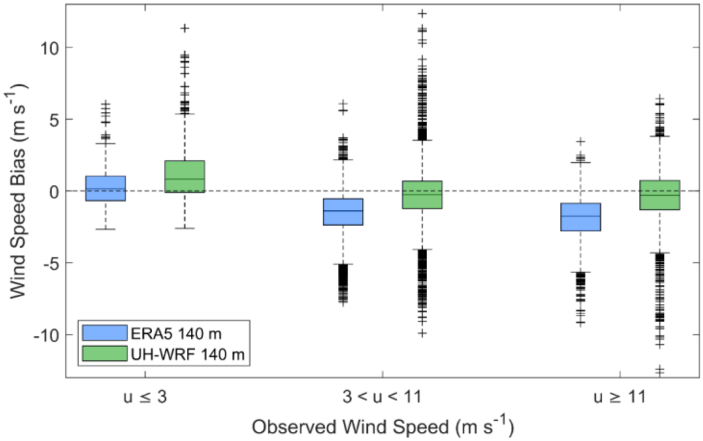

Formatted: Centered

Figure 54. ERA5 and UH-WRF wind speed bias according to observed wind speed during the ~~Hawaii~~Hawai'i buoy deployment. For this and all box plots in the manuscript, the line in the centre of the box indicates the median.

The seasonal wind cycle during the lidar buoy deployment is characterized by immense variability in the fall and winter and more static conditions in the spring and summer (Figure 6~~Figure 5~~). The observed monthly 140 m wind speed standard deviation is 2.31~~0~~ m s^{-1} for fall and winter months (September – February) and 0.79 m s^{-1} for spring and summer months

(March – August). Especially notable is the steep observed monthly 14~~0~~0 m wind speed increase of 5.66 m s^{-1} between January and February 2023 (Figure 6~~Figure 5~~a); however, i~~. ~~t is important to explore the 2023 seasonal patterns in the context of the long-term patterns. Looking at the monthly wind speeds normalized by the annual average wind speed from the 2023 deployment observations and the simulation datasets, which show similar patterns, in the context of 40 years (1985 to 2024) of normalized monthly 100 m wind speeds from ERA5 (CDS, 2025b), the 2023 seasonal wind speed cycle is atypical relative to the long-term (Figure 6b). While weather events can occur along the eastern shores of O'ahu that alter the typical conditions (Morrison and Businger, 2001) and potentially the temporal wind speed patterns (see Section 3.8), long-term ERA5-based analysis indicates that the 2023 seasonal wind speed cycle at the buoy location is driven by the prevalence of the trade winds (Figure 6c). We find that faster (slower) monthly average wind speeds in 2023, relative to the long-term trends, follow a pattern of increased (decreased) frequency of occurrence of the trade winds (Figure 6b, c). For example, the average wind speed at the buoy location during February 2023 is the 96th percentile of the averages for all Februarys in the 40-year ERA5 record. The frequency of occurrence of the trade winds (50°-100°) during February 2023 (occurring 72% of the time) corresponds to a high percentile relative to all Februarys in the 40-year ERA5 record: 87th. Similarly, the slowest monthly wind speeds in 2023 relative to their 40-year counterparts (January: 9th percentile, March: 18th percentile, October: 4th percentile) have lower frequencies of trade wind occurrences during 2023 (January: 29th percentile, March: 1st percentile, October: 7th percentile) (Figure 6b, c).

Both ERA5 and UH-WRF perform well in capturing the observed monthly wind speed pattern at the Hawai'i buoy location during the year 2023 (Figure 6a, b). When comparing the observed and modelled normalized monthly wind speeds, ERA5 and UH-WRF produce correlations of 0.98 and 0.99, respectively (Figure 6b). The standard deviation of the normalized observed monthly wind speeds is 0.19, while the standard deviations from the models are slightly larger at 0.22 each for ERA5 and UH-WRF.

The reanalysis bias varies throughout the year, with ERA5 exhibiting the largest biases in the spring (March – May 2023, average = -2.01 m s^{-1}), followed by the winter (January, February, December 2023, average = -1.50 m s^{-1}), the fall (September – November 2023, average = -1.41 m s^{-1}), and the smallest biases in the summer (June – August 2023, average = -1.20 m s^{-1}). UH-WRF follows a similar seasonal error pattern as ERA5, with the largest to smallest biases found in spring (-0.39 m s^{-1}), winter (-0.37 m s^{-1}), summer (-0.16 m s^{-1}), and fall (-0.13 m s^{-1}).

Formatted: Superscript

Formatted: Superscript

Formatted: Superscript

Formatted: Superscript

Formatted: Superscript

Formatted: Superscript

Formatted: Superscript

Formatted: Superscript

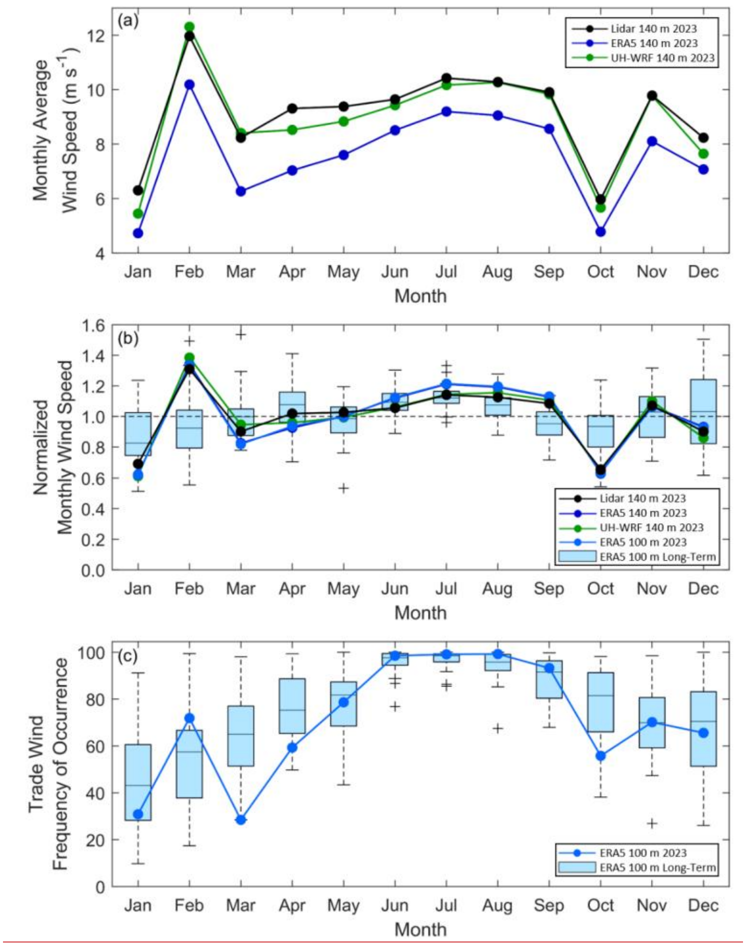

Figure 6. (a) Monthly average wind speeds from the Hawai'i lidar observations, ERA5, and UH-WRF. (b) Monthly average wind speeds normalized by the annual average wind speed from the Hawai'i lidar observations, ERA5, and UH-WRF paired with ERA5 long-term normalized monthly wind speeds, which cover a 40-year period from 1985 to 2024. (c) Frequency of occurrence of winds sourcing between 50° and 100° from ERA5, both long-term and for 2023. Average observed and modelled wind speeds and trade wind frequencies for December reflect only the first half of the month, corresponding to the buoy deployment period.

Formatted: Font: (Default) +Body (Times New Roman)

Formatted: Font: (Default) +Body (Times New Roman)

~~Both ERA5 and UH-WRF perform well in capturing the observed monthly wind speed trends at the Hawaii buoy location. When comparing the observed and modelled normalized monthly wind speeds, ERA5 and UH-WRF produce correlations of 0.98 and 0.99, respectively (Figure 5b). The standard deviation of the observed normalized monthly wind speeds is 0.18 m s^{-1}, while the standard deviations from the models are slightly larger at 0.21 m s^{-1} for ERA5 and 0.22 m s^{-1} for UH-WRF.~~

~~The reanalysis bias varies throughout the year, with ERA5 exhibiting the largest biases in the spring (March – May 2023, average = -1.91 m s^{-1}), followed by the winter (December 2022 – February 2023, average = -1.50 m s^{-1}), the fall (September – November 2023, average = -1.43 m s^{-1}), and the smallest biases in the summer (June – August 2023, average = -1.34 m s^{-1}). UH-WRF follows a similar seasonal error pattern as ERA5, with the largest to smallest biases found in spring (-0.39 m s^{-1}), winter (-0.26 m s^{-1} for January – February 2023), summer (-0.16 m s^{-1}), and fall (-0.13 m s^{-1}).~~

Formatted: Justified, Don't keep with next

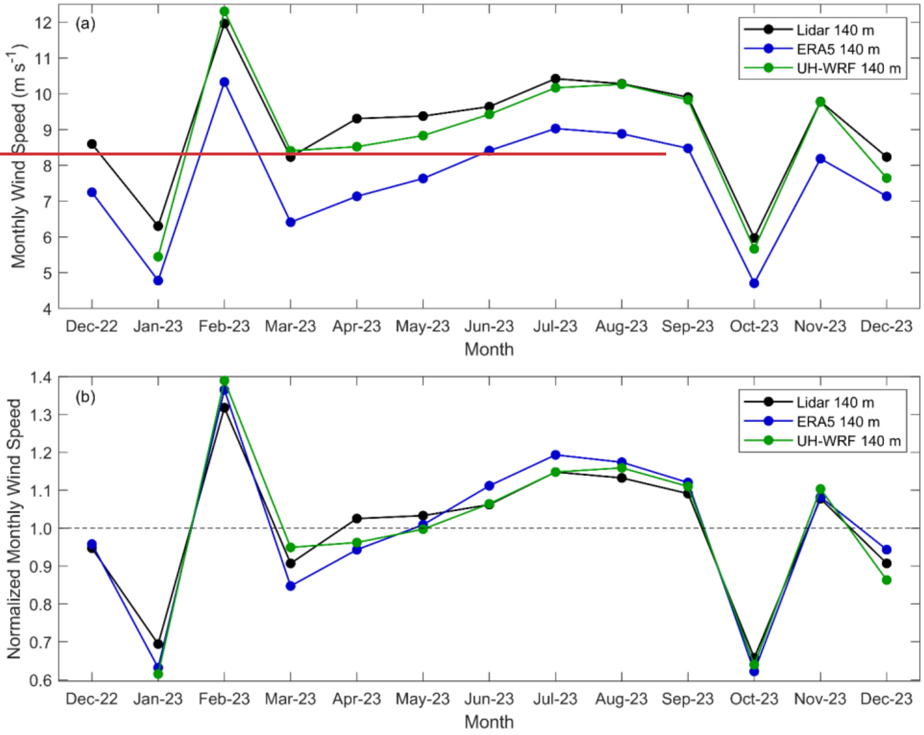

~~Figure 5. (a) Monthly average and (b) normalized monthly average wind speeds from the Hawaii lidar observations, ERA5 and UH-WRF. Average observed and modelled wind speeds for December 2023 reflect only the first half of the month, corresponding to the buoy deployment period.~~

The observed wind speeds transition smooth~~gent~~ly across the diurnal cycle, with a standard deviation of the 140 m hourly average wind speeds of 0.28~~7~~ m s^{-1}. The fastest speeds occur during the evening and at night, while the slowest speeds are observed~~present~~ during the day (Figure 7~~Figure 6~~a, c). The UH-WRF diurnal cycle follows that of the observations, with nearly zero bias occurring for hours between 0 and 11 UTC and underestimation occurring between 12 and 23 UTC (average hourly bias = -0.40~~35~~ m s^{-1}) (Figure 7b). Identifying necessary improvements to better characterize diurnal mixing within boundary layer parameterizations is required. Contrary to ERA5's accurate representation of the observed seasonal wind speed cycle, the reanalysis struggles to capture the observed diurnal cycle in 2023. Trends in the ERA5 wind speeds and associated wind speed biases are tied to the start of the 12-hour reanalysis assimilation windows of 9 and 21 UTC (Hersbach et al., 2020) as shown by the sharp peaks at these hours in Figure 7~~Figure 6~~. Such discontinuities in the ERA5 diurnal wind speed cycle are also noted by Kalverla et al. (2019) over the North Sea. As with the annual and seasonal wind resource, 2023 is an atypical year relative to 40 years of ERA5 diurnal cycles (Figure 7d).~~When comparing the observed and modelled normalized hourly wind speeds, ERA5 and UH-WRF produce correlations of 0.93 and 0.96, respectively (Figure 6c).~~

Formatted: Normal

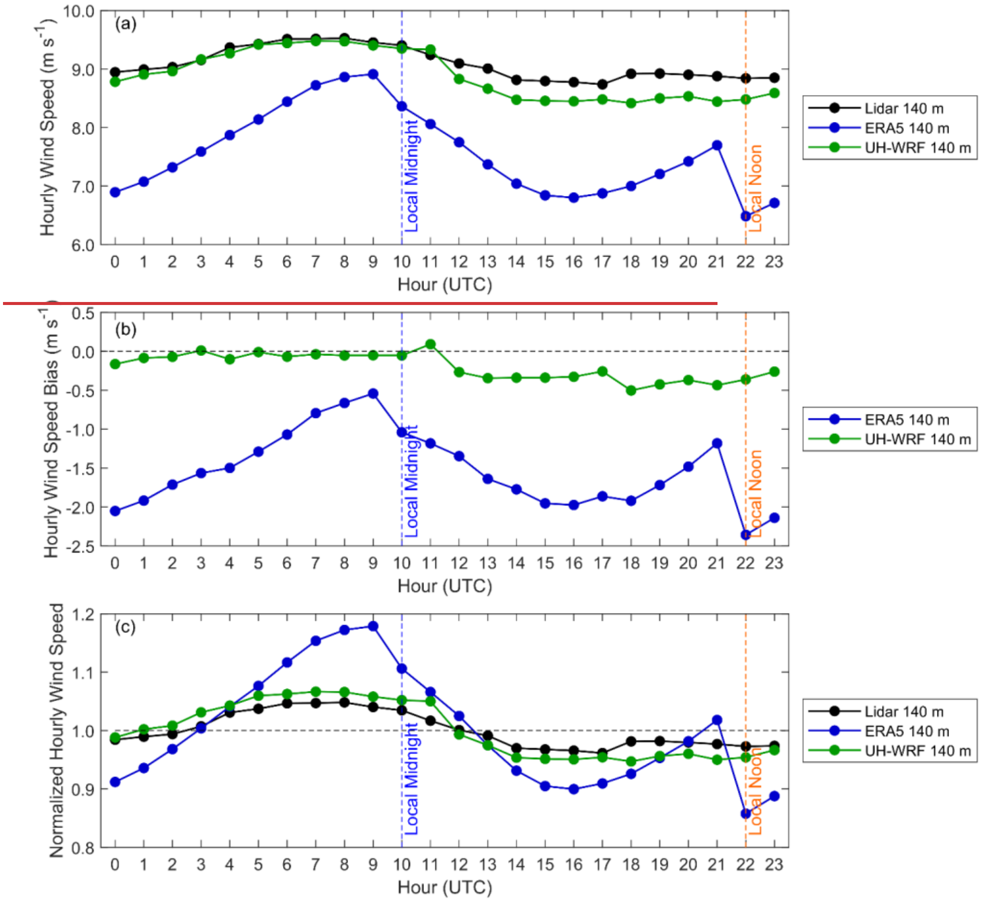
(a)
Hourly Wind Speed (m s^{-1})
10.0
9.0
8.0
7.0
6.0
0 1 2 3 4 5 6 7 8 9 10 11 12 13 14 15 16 17 18 19 20 21 22 23
Hour (UTC)
Local Midnight
Local Noon
Lidar 140 m
ERA5 140 m
UH-WRF 140 m
(b)
Hourly Wind Speed Bias (m s^{-1})
0.5
0.0
-0.5
-1.0
-1.5
-2.0
-2.5
0 1 2 3 4 5 6 7 8 9 10 11 12 13 14 15 16 17 18 19 20 21 22 23
Hour (UTC)
Local Midnight
Local Noon
ERA5 140 m
UH-WRF 140 m
(c)
Normalized Hourly Wind Speed
1.2
1.1
1.0
0.9
0.8
0 1 2 3 4 5 6 7 8 9 10 11 12 13 14 15 16 17 18 19 20 21 22 23
Hour (UTC)
Local Midnight
Local Noon
Lidar 140 m
ERA5 140 m
UH-WRF 140 m

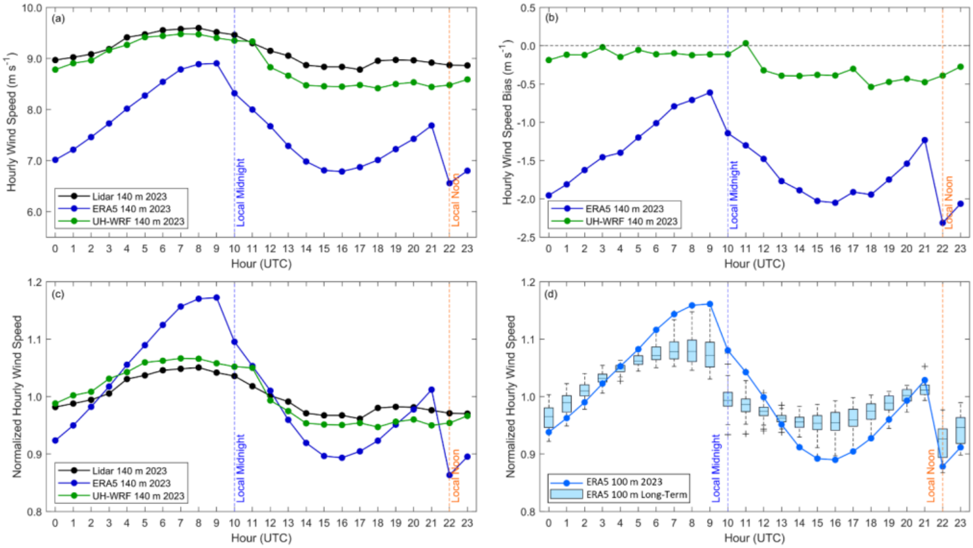

Figure 7~~6~~. (a) Hourly average wind speeds during 2023, (b) hourly wind speed bias during 2023, and ~~and~~ (c) normalized hourly average wind speeds during 2023 from the ~~Hawaii~~Hawai'i lidar observations, ERA5 and UH-WRF. (d) Normalized 2023 and long-term (1985-2024) ERA5 100 m wind speeds at the lidar buoy location.

3.2 Wind dataset performance by wind direction

Formatted: Heading 2

The wind resource in ~~Hawaii~~Hawai'i is dominated by persistent northeast trade winds, with rare occurrences of wind sourcing from the south at ~~Oahu~~O'ahu (Argüeso and Businger, 2018). During the overlapping period of the buoy observations and ERA5 and UH-WRF simulation coverage (1 January 2023 – 15 December 2023), 76% of the observed 140 m wind at the buoy location occur between 50° and 100° (Figure 8a). ERA5 underestimates the observed frequency of winds occurring between 5~~6~~0° and 10~~9~~0° ~~(60%)~~ at 70~~55~~% (Figure 8~~Figure 7~~b), while t~~. During the overlapping period of the buoy observations and the UH-WRF simulation coverage, t~~he percentage of winds occurring between 5~~6~~0° and 10~~9~~0° according to UH-WRF is~~are~~ closer~~very similar~~ to the observations at 73%~~between the two datasets at 61% from UH-WRF versus 62% observed~~ (Figure 8c). Winds originating from O'ahu (230°-300°) (Figure 8a) constitute only 1% of the observed 2023 wind climatology at the lidar buoy location, suggesting that the buoy is situated within the wake of O'ahu island. Both ERA5 and UH-WRF slightly overestimate winds originating from the direction of O'ahu at 3% and 2%, respectively. Winds originating from Moloka'i (110°-150°) are slightly more frequent (3%) and ERA5 and UH-WRF similarly overestimate the rate of occurrence of Moloka'i-based winds at 5%.

~~A small south-southwesterly component of the wind is identified in the lidar buoy observations, with 5% of the wind directions at 140 m occurring between 180° and 210°. While ERA5 captures a south-southwesterly wind component to similar degree, at 4% of the observation period, the reanalysis slightly overrepresents the amount of wind sourcing from the southwest (between 210° and 240°), which includes the southern tip of Oahu (Figure 1a). ERA5 attributes the origin of 3% of the winds to the southwest as compared with less than 2% of the observed winds. During 2023, UH-WRF captures the south-southwesterly frequency (4% observed and simulated) and slightly overrepresents the southwest frequencies (2% versus 1% observed).~~

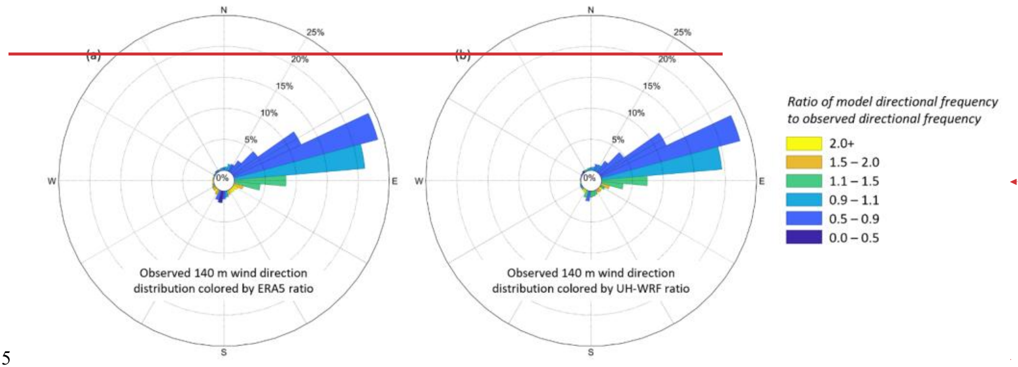

Formatted: Don't keep with next

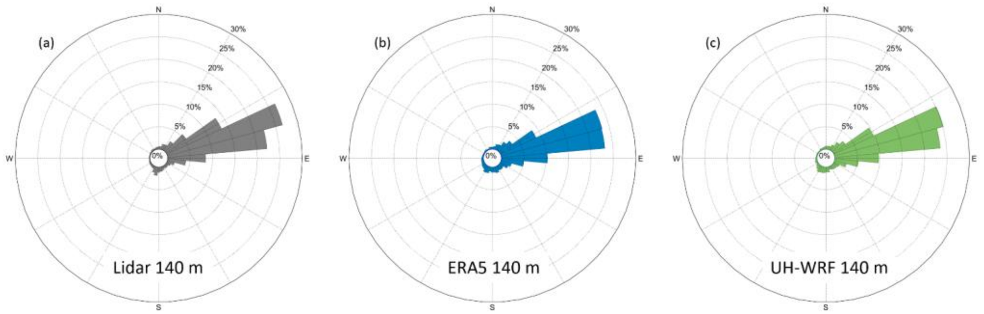

Figure 8~~7~~. W~~Observed w~~ind direction distributions at 140 m from~~ributions coloured by the ratios of~~ (a) the O'ahu lidar buoy,~~ERA5 and~~ (b) ERA5, and (c) UH-WRF between 1 January and 15 December 2023~~UH-WRF directional frequencies to observed directional frequency by sector~~.

As expected given the trade wind-dominant environment, the median 140 m wind speed biases from ERA5 and UH-WRF are extremely similar whether considering the entire buoy deployment period (-1.41 m s^{-1} for ERA5, -0.21 m s^{-1} for UH-WRF) or just times when the trade winds are observed (-1.43 m s^{-1} for ERA5, -0.22 m s^{-1} for UH-WRF) (Figure 9). While

Formatted: Normal

keeping in mind that the sample sizes are significantly smaller when considering island-influenced winds, Figure 9 shows the wind speed biases becoming more positive for winds sourcing from the directions of Moloka'i and O'ahu. For winds originating from Moloka'i, the median ERA5 wind speed bias is -1.01 m s^{-1}, while UH-WRF exhibits a tendency to overestimate the wind speeds with a median bias of 0.46 m s^{-1}. In the rare event that winds at the lidar buoy location originated from O'ahu during 2023, the degree of simulation overestimation is notable, particularly when examining UH-WRF (median wind speed bias = 1.80 m s^{-1}).

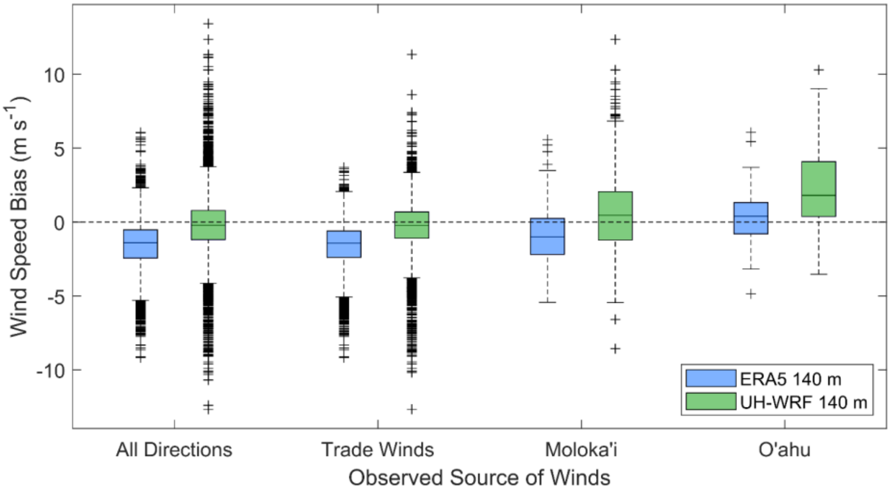

Figure 9. ERA5 and UH-WRF wind speed bias according to observed 140 m wind direction. The trade winds are defined as sourcing between 50° and 100°; Moloka'i-sourced winds are defined between 110° and 150°; O'ahu winds are defined between 230° and 300°.

Formatted: Centered, Keep with next

Formatted: Font: (Default) +Body (Times New Roman)

Formatted: Font: Not Bold

Formatted: Normal

3.3~~2~~ Wind dataset p~~P~~erformance according to turbulence intensity ~~atmospheric stability~~

~~The near surface atmospheric conditions over the Hawaii buoy deployment period are predominantly unstable, with 97% of the period exhibiting cooler air temperatures and warmer sea surface temperatures (Figure 8a). No significant differences in the ERA5 and UH-WRF wind speed biases are noted for distinct atmospheric conditions. Underestimation of the observed wind speeds occurs during unstable and stable conditions, with median ERA5 wind speed biases near -1.50 m s^{-1} regardless of whether the air-sea temperature differential is negative or positive (Figure 8b). For UH-WRF, the median wind speed biases are -0.27 m s^{-1} for unstable conditions and -0.32 m s^{-1} for stable conditions.~~

Assessing the degree of turbulence at a location of wind energy development interest is advantageous for establishing generation expectations, particularly in a waked wind farm environment (Hansen et al., 2011). Therefore, it is important to define the baseline performance of datasets used for wind resource assessment according to different turbulent environments. Using the 1-Hz lidar buoy observations from the Hawai'i deployment (DOE, 2025c), we determine turbulence intensity (*TI*) at turbine hub height using the ratio of the standard deviation to the mean of the 140 m wind speeds over 10-minute periods (DOE, 2025a). At the offshore O'ahu buoy location, *TI* values below 0.1 occur 32% of the deployment period, while the bulk of the measurements (60%) show that *TI* during the deployment is between 0.1 and 0.2 (Figure 10a). The sample size of *TI* values reaching or exceeding 0.2 is small (8% of the deployment period). For hub height wind speeds below 5 m s^{-1}, the observed *TI* at the buoy location follows an inverse relationship with the observed mean 10-minute wind speeds and then hovers around 0.11 for wind speeds faster than 5 m s^{-1} (Figure 10b). ERA5 and UH-WRF exhibit trends of increasingly positive wind speed bias with increasing hub height turbulence, with median ERA5 140 m wind speed biases of -1.63 m s^{-1}, -1.44 m s^{-1}, and -0.18 m s^{-1} and median UH-WRF 140 m wind speed biases of -0.48 m s^{-1}, -0.16 m s^{-1}, and 0.75 m s^{-1} for observed 140 m *TI* less than 0.1, between 0.1 and 0.2, and at least 0.2, respectively (Figure 10c, d).

Formatted: Font: Italic

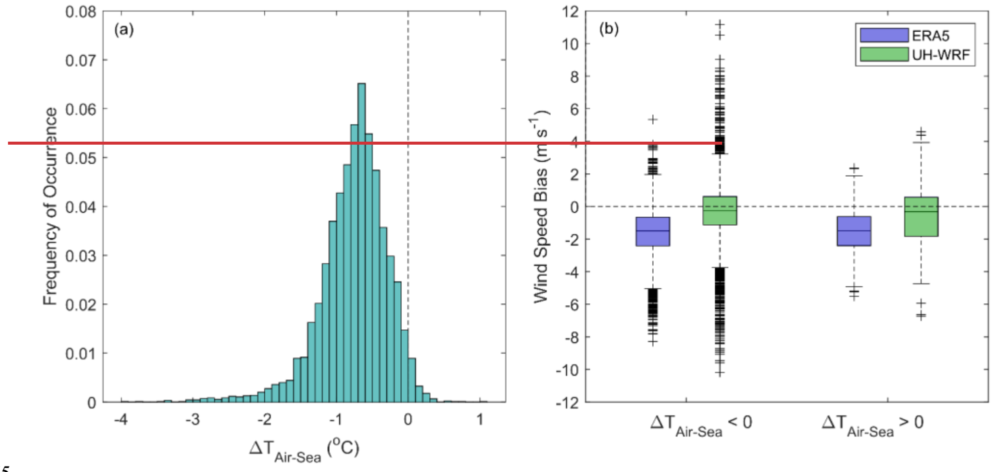
(a)
Frequency of Occurrence
0.08
0.07
0.06
0.05
0.04
0.03
0.02
0.01
0
-4
-3
-2
-1
0
1
ΔT Air-Sea (°C)
(b)
Wind Speed Bias (m s-1)
12
10
8
6
4
2
0
-2
-4
-6
-8
-10
-12
ERA5
UH-WRF
ΔT Air-Sea < 0
ΔT Air-Sea > 0

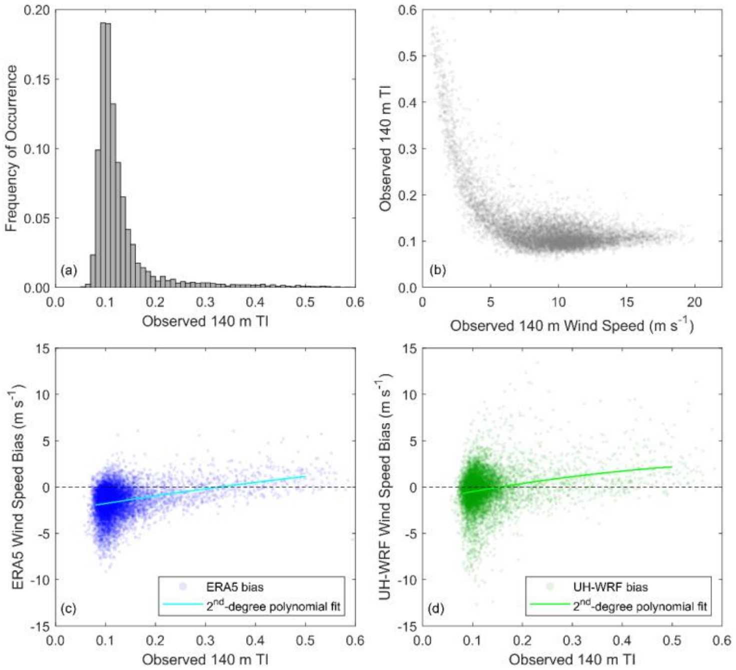

Formatted: Centered

Figure 10~~8~~. (a) Distribution of TI~~t~~ at 140 m~~he air-sea temperature differential~~ during the ~~Hawaii~~Hawai'i lidar buoy deployment,~~.~~ (b) ~~ERA5 and UH-WRF 140 m wind speed bias according to unstable (ΔT < 0°) and stable conditions (ΔT > 0°).~~observed TI according to observed 140 m wind speed, and (c) ERA5 and (d) UH-WRF 140 m wind speed bias according to observed TI.

3.4~~3~~ Wind dataset performance according to wind shear~~ analysis~~

The quantity of power that a wind turbine can produce is influenced by the amount of wind shear across the turbine rotor plane (Wharton and Lundquist, 2012). The ~~Hawaii~~Hawai'i buoy deployment period is characterized by very little shear across the wind profile. Using the wind shear exponent α (Eq. 14) calculated with the lidar wind speeds u_{lo} and u_{hi} at the output heights of z_{lo} = 60 m and z_{hi} = 240 m as our metric, we find that 79~~8~~% of the wind shear exponents during the ~~Hawaii~~Hawai'i deployment fall within ±0.05, compared with 43% of the central California and only 16% of the northern California deployments. ERA5 and UH-WRF, which similarly provide wind speed data at z_{lo} = 60 m and z_{hi} = 240 m, estimate even less wind shear across the profile. ERA5 and UH-WRF predict~~s~~ 84~~6~~% and 88%, respectively, of the wind shear exponents during the ~~Hawaii~~Hawai'i deployment to fall within ±0.05 ~~. During 2023, UH-WRF also predicts 88% of~~

~~the wind shear exponents to fall within ±0.05, compared with 79% based on the lidar observations~~ (Figure 11~~Figure 9~~a, b). The ERA5 and UH-WRF wind speed biases tend to be negative during periods of observed negative and near-zero wind shear and become increasingly positive with larger shear exponents (Figure 11~~Figure 9~~c).

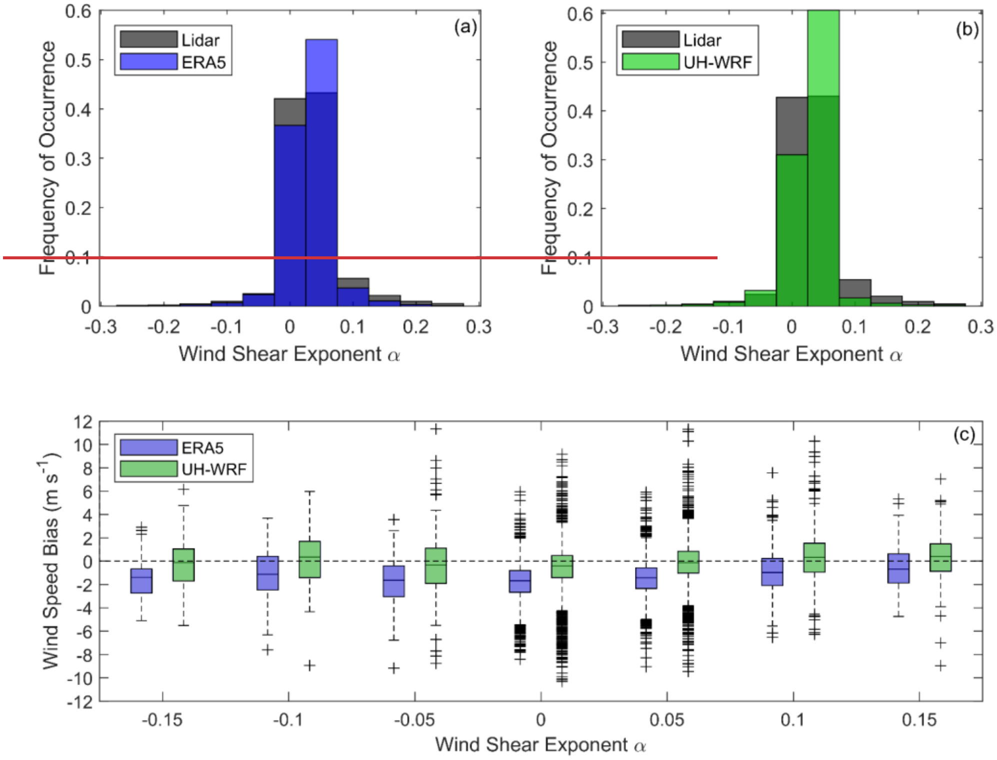
(a)
Lidar
ERA5
Frequency of Occurrence
0.6
0.5
0.4
0.3
0.2
0.1
0
-0.3
-0.2
-0.1
0
0.1
0.2
0.3
Wind Shear Exponent α
(b)
Lidar
UH-WRF
Frequency of Occurrence
Wind Shear Exponent α
(c)
ERA5
UH-WRF
Wind Speed Bias (m s^{-1})
12
10
8
6
4
2
0
-2
-4
-6
-8
-10
-12
-0.15
-0.1
-0.05
0
0.05
0.1
0.15
Wind Shear Exponent α

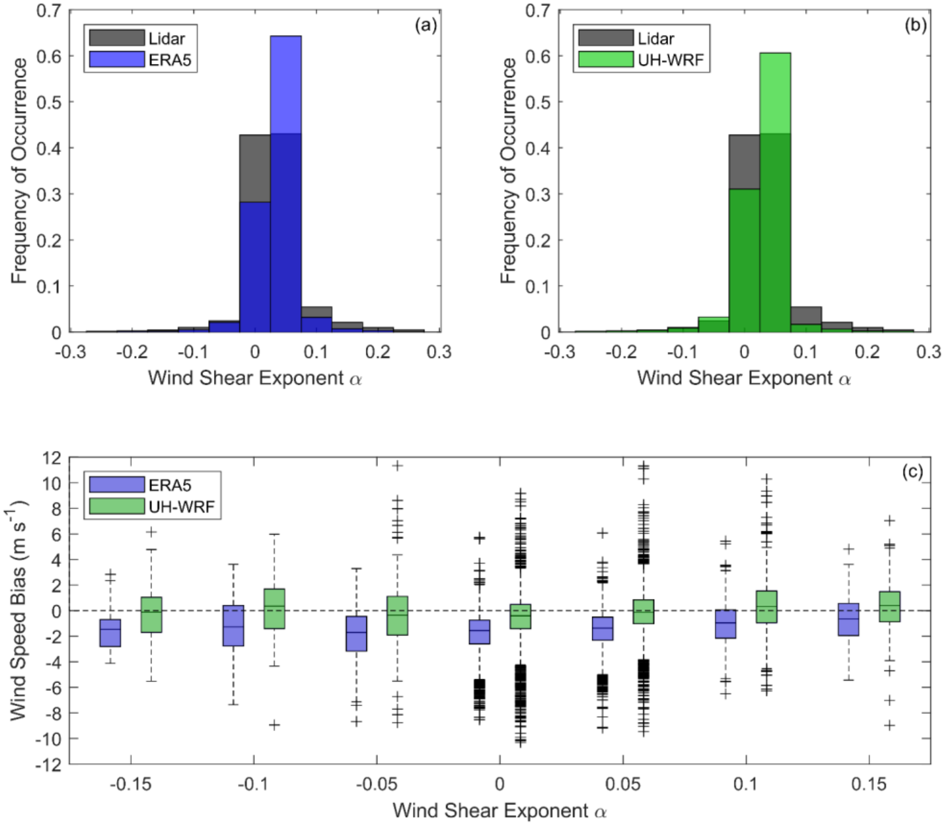

Figure 11~~9~~. Distribution of observed and (a) ERA5 and (b) UH-WRF wind shear between 60 m and 240 m during the ~~Hawaii~~Hawai'i lidar buoy deployment. (c) ERA5 and UH-WRF wind speed bias according to observed wind shear exponent.

3.5 Wind dataset performance according to cloud conditions

The presence of clouds, and the ability of simulation datasets to account for them, can impact the accuracy of wind speed estimates. For example, Lee et al. (2025) find that rotor layer wind speeds at two locations offshore of California, United States are generally stronger under clear sky conditions and that the High-Resolution Rapid Refresh model exhibits a smaller bias under cloudy conditions. During the O'ahu deployment, the lidar buoy was equipped with a pyranometer that allows for estimation of the cloud mask and cloud optical thickness (Appendix A3.4) (DOE, 2025b). A pyranometer outage occurred

Formatted: Normal

between 10 January and 17 March 2023 (DOE, 2025b). Of the period when the wind speed and pyranometer observations, along with the ERA5 and UH-WRF simulations, are available, 42% of the analysis period is characterized by clear sky conditions and 58% by cloudy conditions (Figure 12a). When comparing clear versus cloudy periods, we find the opposite results of Lee et al. (2025): the O'ahu 140 m observed wind speeds are generally stronger during cloudy periods (median = 9.75 m s^{-1}) than during clear sky periods (median = 8.57 m s^{-1}) (Figure 12b). This is primarily due to the presence of stratocumulus cloud conditions over California, which generally suppress turbulence and vertical mixing, reducing wind speeds, in contrast to trade wind cumulus clouds near Hawai'i, which are associated with stronger winds and increased convection. At the O'ahu location, ERA5 performs slightly worse during cloudy conditions in representing the observed 140 m wind speeds (median bias = -1.52 m s^{-1} for clear sky periods versus -1.69 m s^{-1} for cloudy periods), whereas UH-WRF performs similarly regardless of the presence of clouds (median bias = -0.35 m s^{-1} for clear sky periods versus -0.33 m s^{-1} for cloudy periods) (Figure 12c, d).

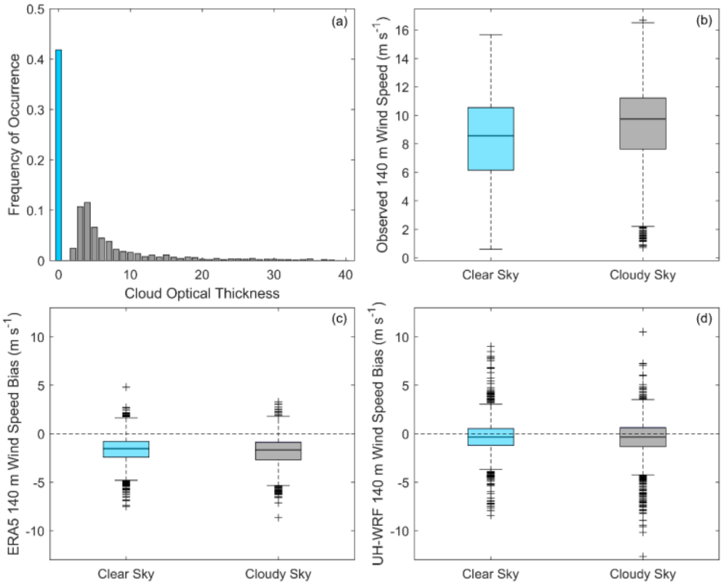

Figure 12. (a) Estimated cloud optical thickness based on pyranometer measurements from the lidar buoy deployment. (b) Observed 140 m wind speed, (c) ERA5 140 m wind speed bias, and (d) UH-WRF 140 m wind speed bias according to clear versus cloudy sky conditions.

Formatted: Centered, Keep with next

Formatted: Font: Not Bold

Formatted: Caption

3.6 Wind dataset performance according to ocean conditions

Over bodies of water, wave fields impact surface momentum fluxes and therefore wind speed profiles (Edson et al., 2013). While some exploratory research has been performed to evaluate the role of wind/wave interactions on wind profiles, most predictive models used for wind resource assessment do not predict the wave fields, instead relying on parameterizations to represent their effects (Gaudet et al., 2022; 2024). Wave measurement at the lidar buoy location begins 17 March 2023 and continues uninterrupted through the remainder of the deployment (Appendix A3.3). During the overlapping period of the wind and wave observations and the ERA5 and UH-WRF simulations, significant wave heights between 1 m and 2 m occur most frequently (63% of the period) (Figure 13a). A positive correlation is noted between observed significant wave height and the 140 m wind speed, though the weakest wind speeds occur when the significant wave heights meet or exceed 1 m (Figure 13b).

Regardless of lidar measurement height, no trends in the ERA5 wind speed performance emerge according to significant wave height, with median ERA5 wind speed biases of -1.72 m s^{-1}, -1.31 m s^{-1}, -1.58 m s^{-1}, and -1.27 m s^{-1} at the closest lidar height to the surface (60 m) corresponding to significant wave heights of 0-1 m, 1-2 m, 2-3 m, and 3-4 m (Figure 13c). At all lidar measurement heights, the UH-WRF wind speed biases become increasingly positive with increasing wave height, with median wind speed biases at 60 m of -0.49 m s^{-1}, -0.32 m s^{-1}, -0.34 m s^{-1}, and -0.02 m s^{-1} corresponding to significant wave heights of 0-1 m, 1-2 m, 2-3 m, and 3-4 m (Figure 13d).

Formatted: Normal

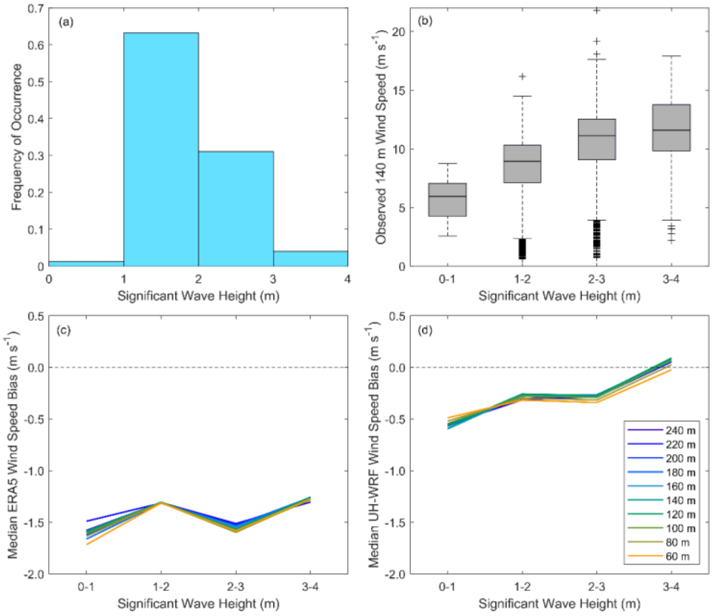

Figure 13. (a) Significant wave height measurements from the lidar buoy deployment. (b) Observed 140 m wind speed, (c) median ERA5 wind speed bias from 60-240 m, and (d) median UH-WRF wind speed bias from 60-240 m according to significant wave height.

Formatted: Keep with next

3.7~~4.2~~ R~~NOW-23 r~~epresentation of ramp events

Observed wind ramp events are present at the Hawaii buoy deployment location, though not plentiful. Following the study of Bianco et al. (2025), we determine the amplitude of the change in the wind energy capacity factor, *ΔCF*, using the rotor equivalent wind speeds as defined by Wagner et al. (2014) from the lidar, ERA5, and UH-WRF~~ and NOW-23~~ with the NREL 15 MW offshore wind reference power curve (Musial et al., 2019), over a duration *Δt*. For this study, we consider *ΔCF* ≥ 40 percentage points~~0.4~~ over *Δt* = 1-3 hours~~ 10 minutes~~ that occur~~hrough~~ during the analysis period 1 January – 15 December 2023 (Figure 14)~~ December 2022 – November 2023~~. ~~The year-long observations produce slightly more up ramps (56) than down ramps (42), for a total of 98 ramps. The annual ramp estimates from NOW-23 are very similar to the observed at a median of 102 total ramps, though the median annual amount of up (down) ramps is slightly higher (lower) at 64 (38) (Figure 14).~~It is important to note that shorter ramp events with smaller values of *ΔCF* can also be counted as part of longer ramp events with larger values of *ΔCF* (e.g., a ramp with a 40-percentage point *ΔCF* over 1 hour could be part of a ramp with a 60-percentage point *ΔCF* over 2 hours).

Over the 1-year analysis period, ramp events represent a small fraction of the observations. Ramps over 1, 2, and 3 hours occur 2%, 3%, and 5% of the period when the observations are available, respectively (Figure 14a). ERA5 (Figure 14b) and UH-WRF (Figure 14c) perform similarly to each other in representing slightly less frequent ramp occurrences with ramp event frequencies of 1%, 2%, and 3% over 1, 2, and 3 hours, respectively. Future work will explore the models' accuracy in representing ramp events in terms of timing, duration, and magnitude.

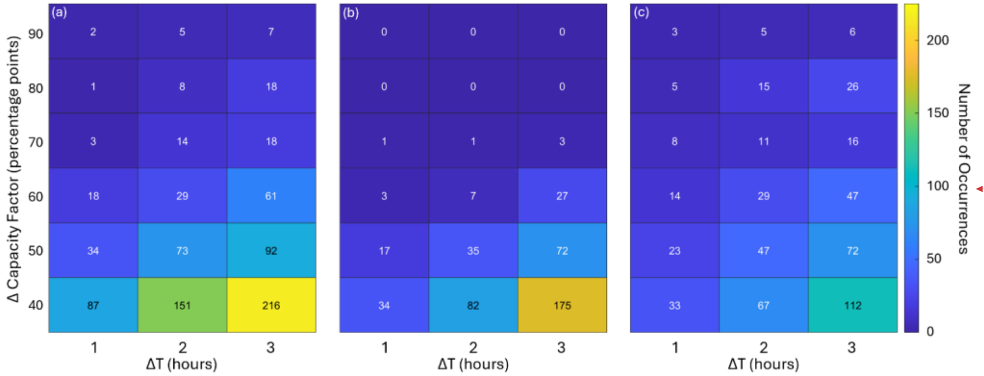

Figure 14. Occurrences of (a) observed, (b) ERA5, and (c) UH-WRF wind ramps (combined up and down) defined by a change in capacity factor of at least ±40 percentage points over 1-3 hours.

3.84 Extreme weather events

While the eastern shores of O'ahu are dominated by persistent trade winds, extreme weather events can occur that alter the typical conditions and potentially the performance of wind simulation datasets. Several events, ranging from Kona lows to a hurricane, impacted the wind resource at the buoy location during the deployment period, allowing for analysis of the performance of ERA5 and UH-WRF in representing such events.

~~August 2023 Hawaii wind event~~

~~On 8 August 2023, stronger than normal northeast trade winds impacted the Hawaiian Islands and were a contributing factor in the fires that devastated the city of Lahaina on Maui (Mass and Ovens, 2024). On the same date, Hurricane Dora passed to the south of the islands (Bucci, 2024). To the east of the islands at the lidar buoy location, the observed and modelled winds shift further east-southeast from around 60° to 80° on 6 August (Figure 10b). Beginning on 7 August at 15 UTC, the buoy measurements capture a ramp event when the 140 m wind speed increases by 6.63 m s^{-1} over the course of 5 hours (Figure 10a). ERA5 produces an increase in the 140 m wind speed beginning 1 hour later with a smaller magnitude ramp (4.42 m s^{-1}). The UH-WRF simulation shows an increase of 3.42 m s^{-1} over 4 hours beginning at 15 UTC, followed by a stronger up~~

Formatted: Keep with next

Formatted: Caption

Formatted: Font: (Default) +Body (Times New Roman)

Formatted: Font: Not Bold

Formatted: Normal

~~ramp a few hours later. ERA5 and UH-WRF have similar and lower correlations, respectively, during the event (0.89 and 0.81) versus the entire deployment (0.89 and 0.85). The ERA5 and UH-WRF wind speed biases at 140 m are smaller during the event relative to the entire deployment (-1.36 m s^{-1} versus -1.53 m s^{-1} for ERA5 and 0.03 m s^{-1} versus -0.25 m s^{-1} for UH-WRF).~~

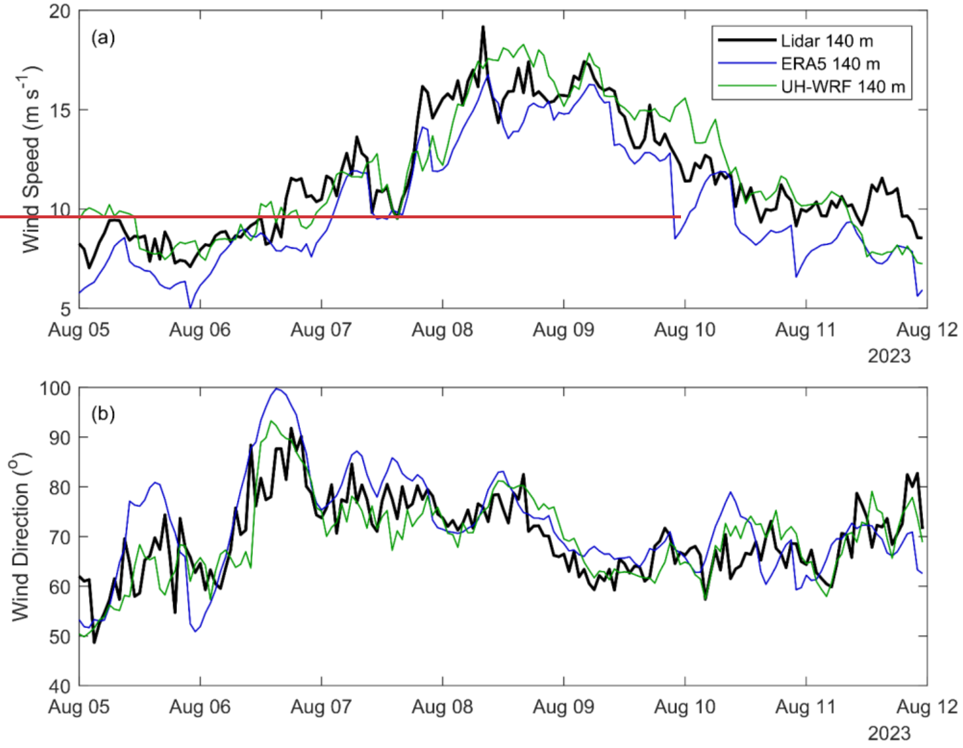

~~**Figure 10.** Observed and modelled (a) wind speeds and (b) wind directions at the lidar buoy location during the August 2023 Hawaii wind event.~~

3.8.1 February 2023 Kona lows

Two consecutive Kona lows (Morrison and Businger, 2001) developed near the Hawaiian Islands in mid-February 2023, resulting in heavy rainfall impacts on several islands (NOAA, 2023a). The buoy observations during this period confirm the disruption of the easterly trade winds, with wind directions becoming more variable and wind speeds weakening (Longman et al., 2021). No extreme wind events are recorded by the buoy during the Kona low events; rather, the wind speeds are elevated during the trade wind dominant periods before and after the events (Figure 15a).

While both simulation datasets capture the decrease in wind speed (Figure 15a) and shift in wind direction from the dominant easterly pattern (Figure 15b), they struggle with representing the temporal variations in the wind speeds during the Kona low events. ERA5 and UH-WRF produce notably lower correlations during the low events between 15-19 February (0.63 and 0.46) relative to the entire deployment (0.89 and 0.85). The ERA5 wind speed biases at 140 m are smaller during the Kona low events relative to the entire deployment (-1.34 m s^{-1} versus -1.54 m s^{-1}), while UH-WRF overestimates the observed wind speeds during the events at a greater magnitude than the model underestimates the observed wind speeds during the entire deployment (0.46 m s^{-1} versus -0.25 m s^{-1}). Following the Kona low on 19 February, ERA5 simulates lower wind speeds for an extended period (19-25 February) compared to the observations. This could be attributed to several factors, including challenges in data assimilation after the Kona event, residual atmospheric instabilities delaying boundary layer recovery, misinterpretation of sea surface temperatures and moisture fluxes, or limitations in model physics and parameterizations. Further analysis will be addressed in upcoming work.

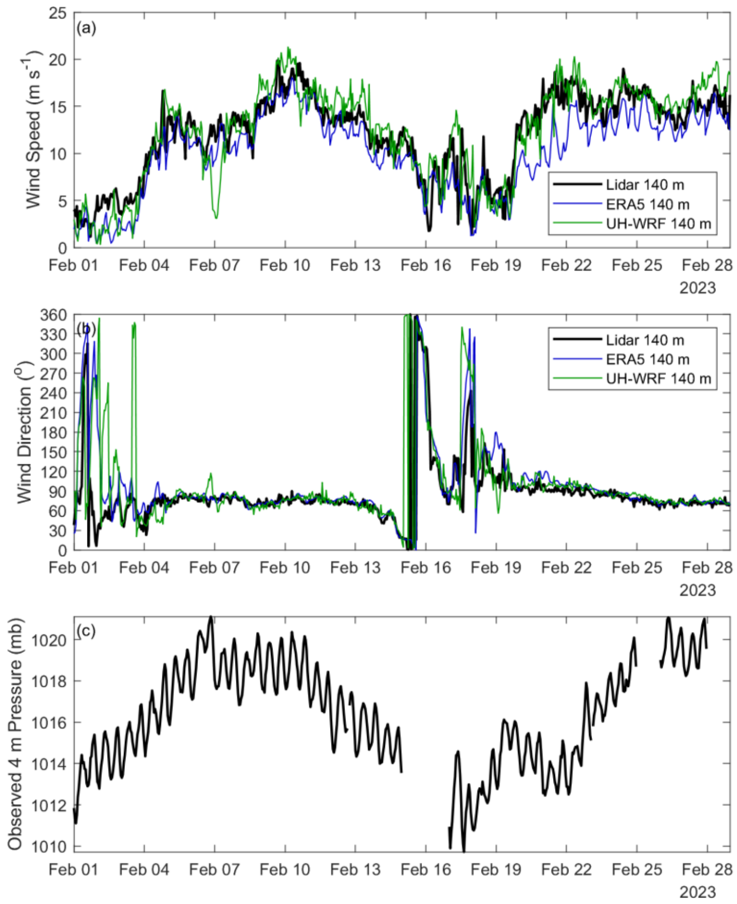

Figure 15. Observed and modelled (a) wind speeds and (b) wind directions and (c) observed 4 m air pressure at the lidar buoy location during February 2023.

3.8.2 April 2023 frontal passage

The maximum 140 m wind speed recorded by the buoy is 21.8 m s^{-1}, which occurred on 19 April 2023 and is associated with the passage of a strong cold front (NOAA, 2023b). Despite this event, which is captured by ERA5 and UH-WRF with

Formatted: Keep with next

Formatted: Font: Not Bold

Formatted: Caption

varying degrees of success (Figure 16), long-term ERA5 analysis indicates that the monthly average wind speed for April 2023 is within the 22nd percentile when considering all Aprils in the past 40 years (Figure 6b), implying that the frontal passage has little impact on the overall monthly wind resource.

Formatted: Superscript

As the pressure drops on 18 April, both ERA5 and UH-WRF miss an initial spike in the observed 140 m wind speed at 20 UTC that reaches 12.4 m s^{-1} (Figure 16a). This discrepancy may be due to limitations in capturing rapid changes in pressure gradients that drive localized wind accelerations during the initial stages of the event. The maximum observed 140 m wind speed of 21.8 m s^{-1} occurs 16 hours later on 19 April at 12 UTC, likely driven by the strengthening of the pressure gradient and subsequent momentum transfer through heightened vertical mixing. While ERA5 simulates a peak at the same hour, it significantly underestimates the wind speed at 15.7 m s^{-1}, potentially due to coarse spatial resolution and weaker representation of boundary layer turbulence and mixing processes. UH-WRF, with its finer resolution and more detailed boundary layer parameterization, captures a closer estimate of the peak wind speed at 19.2 m s^{-1}; however, the model exhibits a 3-hour delay, peaking at 15 UTC (Figure 16a). This delay may result from inaccuracies in simulating the timing of mesoscale dynamics, such as propagating pressure disturbances and their interaction with local islands. Similar to the Kona low event on 19 February, ERA5 exhibits significant bias following the frontal passage, highlighting challenges with the model's representation and underlying physics.

Formatted: Centered, Keep with next

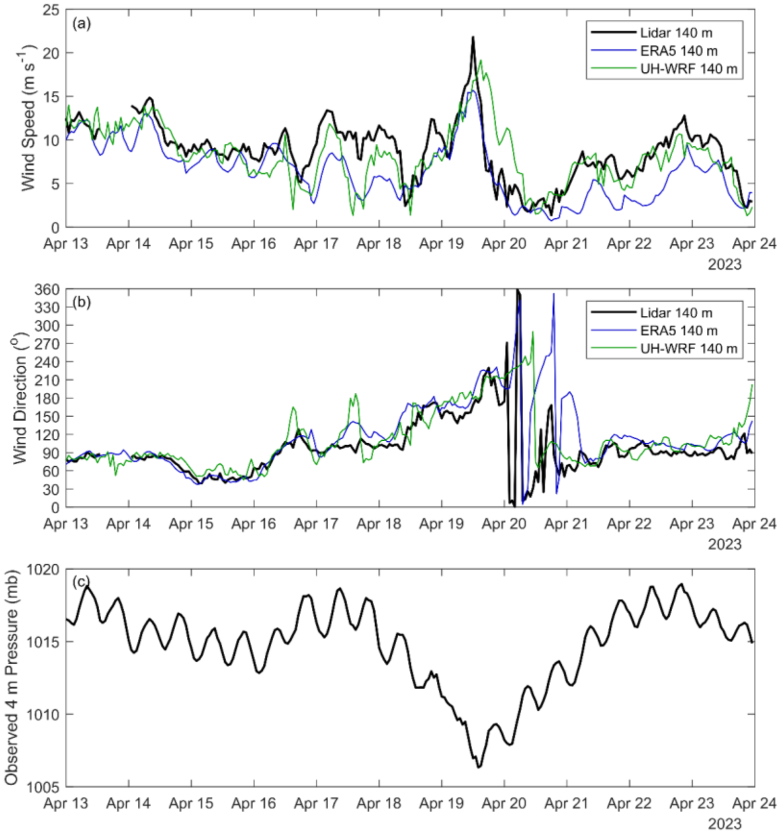

Figure 16. Observed and modelled (a) wind speeds and (b) wind directions and (c) observed 4 m air pressure at the lidar buoy location during 13-23 April 2023.

3.8.3 August 2023 Hawai'i wind event and Hurricane Dora

On 8 August 2023, stronger than normal northeast trade winds impacted the Hawaiian Islands and were a contributing factor in the fires that devastated the city of Lahaina on Maui (Mass and Ovens, 2024). On the same date, Hurricane Dora passed to the south of the islands (Bucci, 2024). The wind ramp event highlights the complex interplay between Hurricane Dora's circulation and stronger-than-normal northeast trade winds, which intensified the regional pressure gradient and drove anomalous east-southeast wind patterns at the lidar buoy location.

East of the islands at the lidar buoy location, the observed and modelled winds shift further east-southeast from around 60° to 80° on 6 August (Figure 17b). Beginning on 7 August at 15 UTC, the buoy measurements capture a ramp event when the 140 m wind speed increases by 6.63 m s^{-1} over the course of 5 hours (Figure 17a). The rapid increase in wind speeds can be attributed to enhanced vertical momentum transfer through turbulent mixing and boundary layer dynamics, likely exacerbated by the interaction of hurricane-induced pressure gradients and persistent trade wind surges. ERA5 simulates an increase in the 140 m wind speed starting 1 hour later, with a less pronounced ramp (4.24 m s^{-1}). The UH-WRF simulation depicts an increase in the 140 m wind speed of 3.42 m s^{-1} over a 4-hour period starting at 15 UTC, followed by a stronger up ramp later. Correlations for ERA5 and UH-WRF during the event are similar and slightly lower, respectively, compared to the entire deployment, at 0.90 and 0.81 versus 0.89 and 0.85. Wind speed biases at 140 m during the event are smaller relative to the overall deployment, with ERA5 showing a bias of -1.34 m s^{-1} versus -1.54 m s^{-1} and UH-WRF exhibiting a bias of 0.03 m s^{-1} versus -0.25 m s^{-1}. While both ERA5 and UH-WRF partially captured the event, discrepancies in timing and magnitude underscore limitations in turbulent mixing, boundary layer representation, and resolution, particularly when simulating mesoscale processes in complex terrain or offshore environments. Understanding the interaction between synoptic and mesoscale forces during extreme events like this provides critical insight into improving atmospheric modelling techniques for future studies.

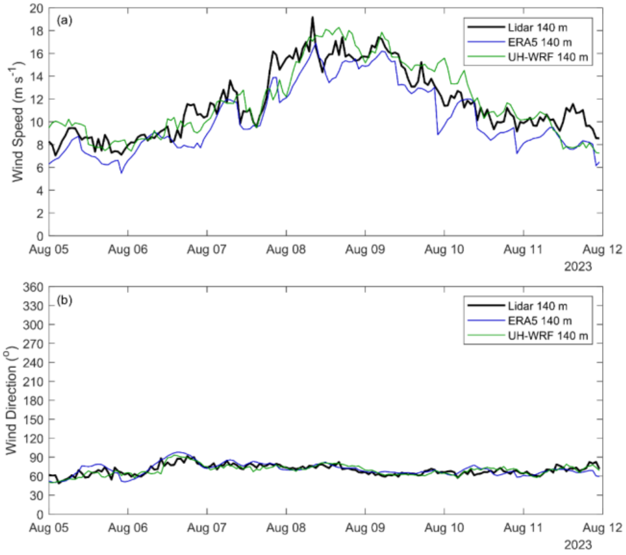

Figure 17. Observed and modelled (a) wind speeds and (b) wind directions at the lidar buoy location during the August 2023 Hawai'i wind event.

~~4 Long-term model evaluation~~

~~This study proceeds to analyse the performance of two additional wind resource datasets off the coast of Oahu, NOW-23 and GWA3, while acknowledging the significant limitation that these datasets do not temporally coincide with the lidar buoy observation period (1 December 2022 – 15 December 2023). Therefore, we utilise the entire temporal coverage periods of NOW-23 (2000 – 2019) and GWA3 (2008 – 2017) to determine whether the observed wind speeds and the seasonal and diurnal wind speed trends are represented in the ranges of simulated long-term wind speeds. Given the higher temporal resolution of NOW-23, we additionally explore whether the occurrences of LLJs and ramp events are captured in the ranges of simulated long-term wind speeds for this dataset. The year-long period of 1 December 2022 – 30 November 2023 is used for the observational point of comparison in the following analyses. As for the temporally concurrent assessments of ERA5 and UH-WRF, the analysis of NOW-23 and GWA3 considers the wind profile up to 240 m plus a focused investigation at 140 m. GWA3 wind speed estimates are adjusted to 140 m following Eq. 4 and 5.~~

Formatted: Centered

Formatted: Font: Not Bold

~~4.1 Annual, seasonal, and diurnal representation~~

~~Across the wind profile between 60 m and 240 m, the observed annual average wind speeds during the year-long Hawaii deployment fall within the 25th and 75th percentiles of the annual average wind speeds simulated by NOW-23 and GWA3, though at distinct percentiles within that range (Figure 11). At 140 m a.s.l., the observed annual average wind speed during the period of December 2022 – November 2023 (9.12 m s^{-1}) is aligned with the 28th percentile annual average wind speed from NOW-23 over the full dataset period of 2000 – 2019. The median and average 140 m NOW-23 annual average wind speed estimates over the full dataset period are 9.43 m s^{-1} and 9.52 m s^{-1}, respectively. The observed annual average wind speed at 140 m coincides with the 57th percentile annual average wind speed for GWA3 during its coverage period of 2008 – 2017 (Figure 11b). The median and average 140 m GWA3 annual average wind speed estimates over the dataset coverage period are 9.06 m s^{-1} and 9.02 m s^{-1}. Using the long-term annual average 140 m wind speed from NOW-23 produces a smaller magnitude bias (+0.39 m s^{-1}) than using ERA5 (-1.53 m s^{-1}), while GWA3 produces a smaller magnitude bias (-0.10 m s^{-1}) than both ERA5 and UH-WRF (-0.25 m s^{-1}), despite the temporal concurrency with the observations of the latter two products.~~

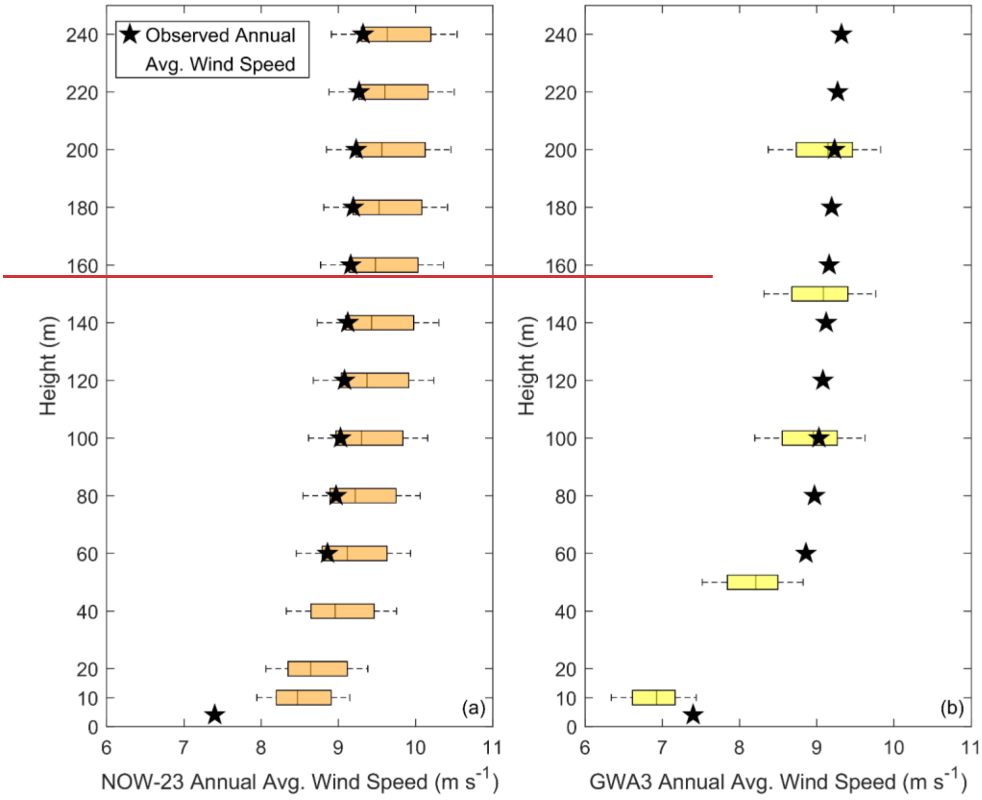

~~**Figure 11.** (a) NOW-23 (2000 – 2019) and (b) GWA3 (2008 – 2017) annual average wind speeds with observed annual average wind speeds (1 December 2022 – 30 November 2023).~~

~~The month-to-month variability in the observed 140 m wind speeds during the deployment year are not well captured by the monthly wind speed indices provided by GWA3 or the median monthly 140 m wind speeds from NOW-23, with correlations of 0.40 and 0.29, respectively (Figure 12). GWA3 and NOW-23 are generally in agreement (correlation of 0.72 between the two datasets) that the slowest wind speeds east of Oahu occur in the winter and the fastest wind speeds occur in the summer, but the average observed winds during the year of deployment exhibit several significant inconsistencies between months, particularly during the periods December 2022 through April 2023 and September through November 2023 (Figure 12).~~

~~The range of the normalized observed wind speeds during the deployment year (0.65 in October 2023 to 1.31 in February 2023) exceeds those from GWA3 (0.83 in January to 1.10 in June) and the median of the 20-year NOW-23 dataset (0.89 in January to 1.11 in July). However, when considering all 20 years in the NOW-23 Hawaii dataset, normalized wind speeds at the location of the DOE buoy are estimated to reach extents of 0.50 and 1.45, with the upper estimate occurring the same month as the fastest observed wind speeds, February (Figure 12). Performing a Student's t-test with a 5% significance level finds that December 2022, March and April 2023, June and July 2023, and November 2023 are within the variability of the NOW-23 climatologies.~~

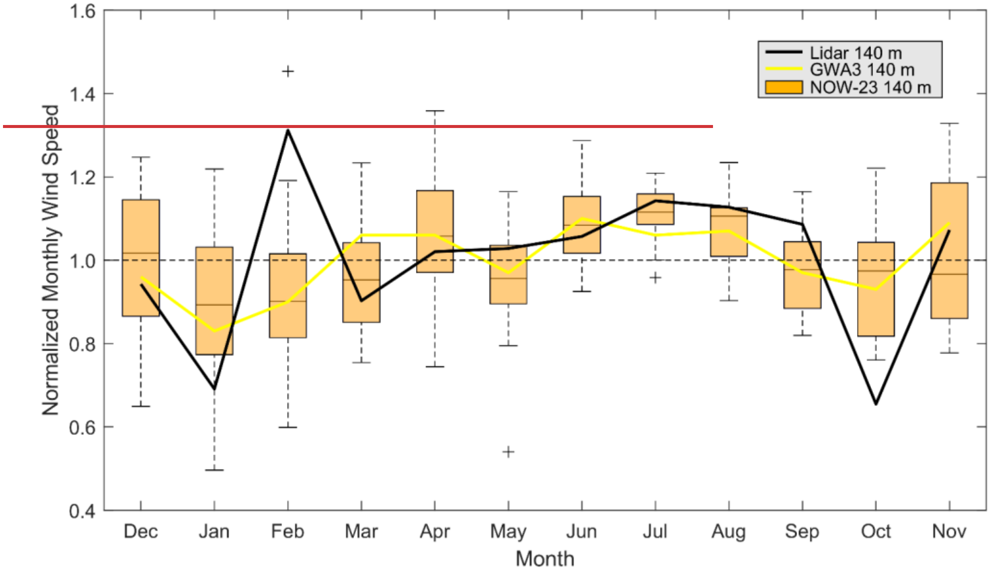

~~**Figure 12.** Normalized monthly wind speeds from the Hawaii deployment lidar (December 2022 – November 2023), GWA3 (2008 – 2017), and NOW-23 (2000 – 2019).~~

~~Conversely to the misalignment between the observed and simulated seasonal trends in the 140 m wind speed at the Hawaii buoy deployment location, the observations, NOW-23, and GWA3 agree that the fastest wind speeds occur during the evening and night and the slowest wind speeds occur during the daytime (Figure 13). The hourly wind speeds from NOW-23 and GWA3 achieve correlations of 0.94 and 0.89 with the observed hourly wind speeds, respectively. The range of normalized wind speeds from the observations (0.96 to 1.05) is slightly greater than that of GWA3 and the median of the 20-year NOW-23 period (0.97 to 1.04 for both datasets). Disagreement between the observations and the datasets is greatest~~

~~between the hours 14 and 17 UTC, the morning transition when the air-sea temperature differential is at its greatest magnitude and begins approaching its smallest magnitude (Figure 13b).~~

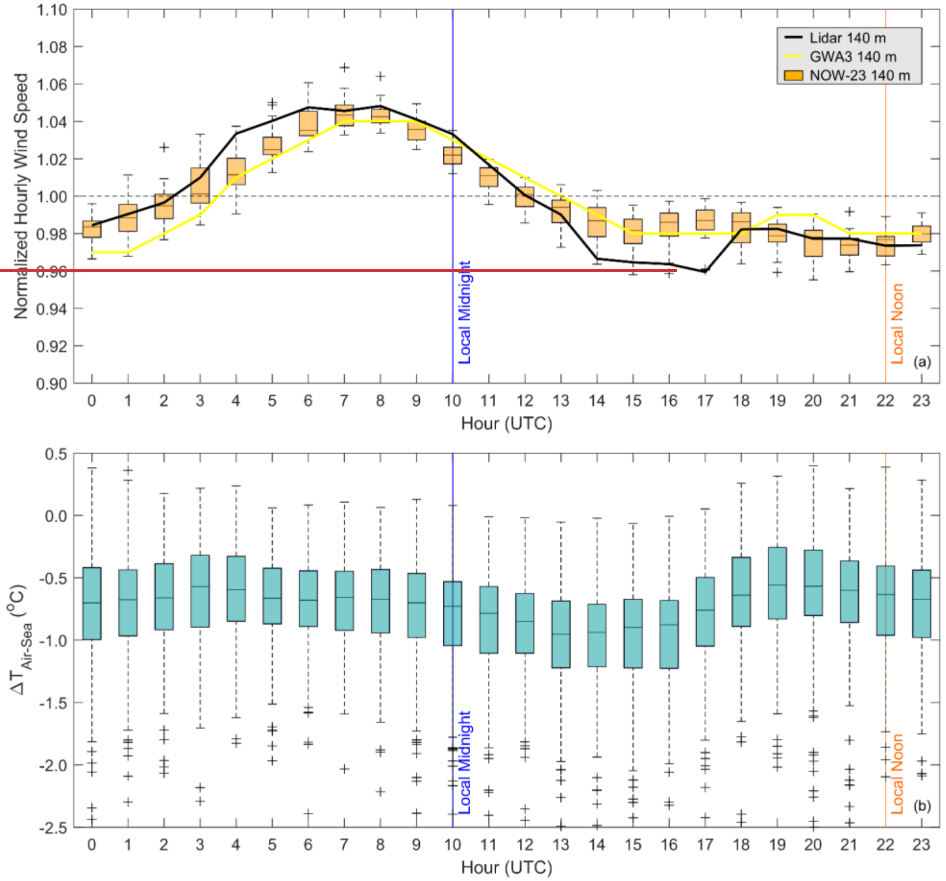

~~**Figure 13.** (a) Normalized hourly wind speeds from the Hawaii deployment lidar (December 2022 – November 2023), GWA3 (2008 – 2017), and NOW-23 (2000 – 2019). (b) Diurnal distribution of the air-sea temperature differential during December 2022 – November 2023.~~

~~4.2 NOW-23 representation of ramp events~~

~~Observed wind ramp events are present at the Hawaii buoy deployment location, though not plentiful. Following the study of Bianco et al. (2025), we determine the amplitude of the change in the wind energy capacity factor, *ΔCF*, using the rotor equivalent wind speeds as defined by Wagner et al. (2014) from the lidar and NOW-23 with the NREL 15 MW offshore wind reference power curve (Musial et al., 2019), over a duration *Δt*. For this study, we consider *ΔCF* ≥ 0.4 over *Δt* = 10 minutes through the analysis period December 2022 – November 2023. The year-long observations produce slightly more up ramps (56) than down ramps (42), for a total of 98 ramps. The annual ramp estimates from NOW-23 are very similar to the observed at a median of 102 total ramps, though the median annual amount of up (down) ramps is slightly higher (lower) at 64 (38) (Figure 14).~~

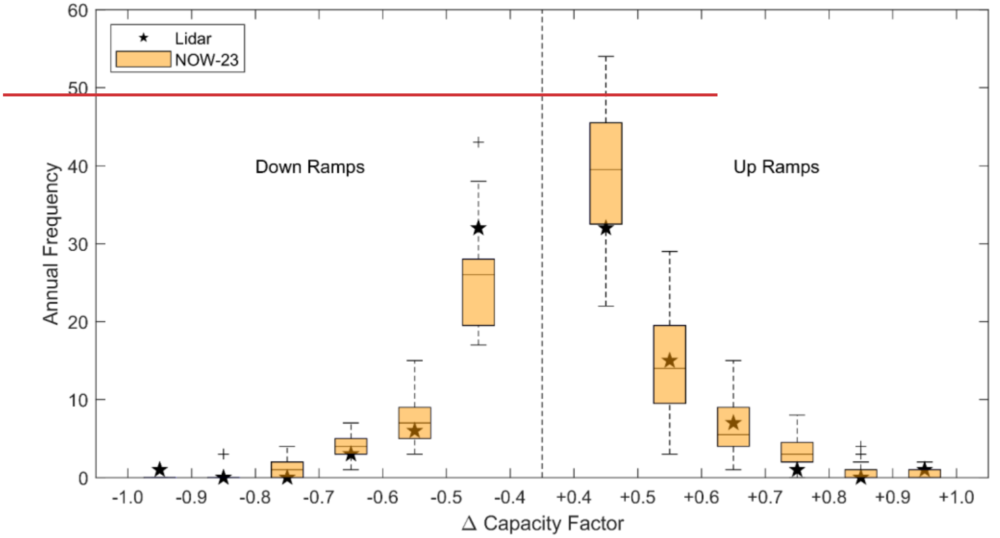

~~**Figure 14.** Annual frequency of observed and NOW-23 100 m wind ramps defined by a change in capacity factors of at least ±0.4 over 10 minutes.~~

4~~5~~ Conclusions~~ and implications for wind energy~~

In this study, we questioned and established the accuracy of a widely-used reanalysis model~~s~~ and a~~,~~ regional model~~s, and purpose-built wind datasets~~ in representation of the observed marine boundary layer~~offshore wind resource~~ in a previously unstudied location off the coast of ~~Oahu~~O’ahu, ~~Hawaii~~Hawai’i using lidar buoy measurements. ~~At a location of future offshore wind development interest due to vast wind resource availability and potential economic impact, the year-long DOE~~

~~lidar buoy deployment off the coast of Oahu highlights the successes and challenges of a widely employed reanalysis and more recent datasets developed to support wind resource characterization.~~ The wind speed biases quantified in this validation provide important baselines for researchers and energy developers~~.~~, offering insights into the performance of models and datasets when estimating the long-term wind resource in the Hawaiian region~~deciding which models and datasets to use and how much to adjust their expectations when estimating the long-term offshore wind resource in the Hawaiian region~~. ~~Given the consistency of the trade wind trends east of Hawaii, we recommend that offshore wind farm planners in this area leverage the datasets found to be successful in this work and adjust their expectations when using datasets that did not perform as well according to their attributes of interest, such as wind speed bias and seasonal and diurnal wind variations.~~This analysis highlights the importance of understanding wind speed bias and variability, including seasonal and diurnal wind trends, to improve characterization of the wind resource in the area.

In particular, the results of this investigation near ~~Hawaii~~Hawai'i corroborate previous reports~~add another geographic data point to the trend~~ of ERA5's underestimation of observed marine boundary layer winds~~offshore wind speeds~~ as documented by Kalverla et al. (2020) over the North Sea, Sheridan et al. (2020) off the coasts of New Jersey and Virginia, United States, Pronk et al. (2022) and Fragano and Colle (2025) off the coast of New Jersey, United States, and Sheridan et al. (2022) off the coast of central California, United States. Given the consistent trade winds at the ~~Oahu~~O'ahu deployment site, we do not attribute the large ERA5 wind speed bias (-1.54~~3~~ m s^{-1}) to the coarseness of the grid leading to mischaracterization of meteorological phenomena such as wind ramps~~ or LLJs~~, simply because the observations yielded so few of these events (Section 3.6), though such errors have shown to be significant at other offshore sites where they are more prevalent (Kalverla et al., 2020; Sheridan et al., 2024). ~~Similarly, we do not identify any performance trends according to atmospheric stability (Figure 8) such as are seen in the work of Pronk et al. (2022), who note the best ERA5 performance across multiple metrics occurring for unstable cases, followed by neutral conditions, and last, stable cases at their offshore study location.~~ Rather, we note that ERA5 significantly underestimates fast wind speeds (Figure 5~~Figure 4~~), which our study site is strongly characterized by (Figure 2~~Figure 2~~). Gandoin and Garza (2024) provide evidence of ERA5's underestimation of fast wind speeds and link the results~~trend~~ to ERA5's representation of the Charnock parameter. We also speculate that the relative sparsity of observations for data assimilation in this remote part of the world could influence the ERA5 error metrics, along with the discontinuities in the diurnal cycle noted in this work (Figure 7~~Figure 6~~) and that of Kalverla et al. (2019). We recommend that users of ERA5 in the vicinity of the ~~Oahu~~O'ahu buoy deployment adjust the initial wind speed and energy generation expectations higher through bias correction (Wilczak et al., 2024) and welcome the use of our publicly available buoy observations (DOE, 2025a, b, c).

Conversely to the challenges noted for ERA5 in terms of wind speed bias, this study underscores the importance of long-term, continuously refined, and dynamically updated reanalysis models. Offshore of O'ahu, the year 2023 exhibited atypical annual average wind speeds (Figure 3b) as well as seasonal and diurnal wind speed variations (Figure 6, Figure 7). Conducting a wind resource assessment based solely on observations from a single year would fail to capture interannual variability, leading to inaccurate wind energy generation estimates for regions east of O'ahu. Combining multi-year observations with simulation datasets provides a more robust and comprehensive baseline understanding of generation expectations.

When financial and computational resources permit~~are available~~, the validation of the UH-WRF simulation in this study~~work~~ highlights~~showcases~~ the advantage~~value~~ of~~ running~~ high~~er~~-resolution regional model~~simulation~~s for~~to~~ improving~~e~~ accuracy in wind resource assessments. The UH-WRF simulations exhibit~~s~~ a significantly smaller bias (-0.25 m s^{-1}) compared to~~than~~ ERA5 and a correlation (0.85) close to~~not far behind that of~~ ERA5 (0.89~~90~~) at the ~~Oahu~~O’ahu site~~, supporting the selection of YSU as the PBL scheme in an additional offshore location (Bodini et al., 2024b)~~. B~~While b~~oth models~~ ERA5 and UH-WRF~~ successfully capture the observed seasonal wind speed cycle driven by changes in large-scale pressure gradients and trade wind trends; however, ~~at the deployment location, ~~UH-WRF excels in resolving~~is superior in capturing~~ the diurnal cycle (Figure 7~~Figure 6~~), which is influenced by localized boundary layer processes such as thermal stratification, land-sea breezes, and turbulent mixing. ~~While such regional simulations as UH-WRF can be temporally limited due to computational expense, researchers have an opportunity to develop long-term estimates by bias-correcting datasets with longer durations with high-quality datasets of shorter duration~~ Despite the limited temporal scope of regional models like UH-WRF due to computational expense, their detailed representation of smaller-scale processes creates opportunities for researchers to refine long-term estimates by bias-correcting extended-duration datasets using high-quality, short-duration simulations (Buster et al., 2024). This combined approach addresses key atmospheric dynamics and enhances confidence in wind resource characterization.

~~Finally, we found it interesting that two datasets that lacked temporal overlap with the Oahu buoy deployment, NOW-23 and GWA3, outperformed ERA5 in terms of bias when simply using their respective long-term annual average wind speeds. However, challenges arise when taking the comparisons to a more granular level, for example, the monthly pattern in the wind observations did not align with the long-term seasonal trends estimated by NOW-23 and GWA3. Additionally, users of GWA3 should be aware that the diurnal wind speed trend is currently available only for 100 m a.s.l. Based on our evaluations and previous offshore wind validations, we recommend performing wind resource assessments using multiple datasets to garner a range of expectations rather than selecting just one product that may result in significant error.~~

Throughout the deployment period, several extreme weather events revealed the performance of ERA5 and UH-WRF in capturing atmospheric conditions offshore of O’ahu. During the February 2023 Kona lows, trade wind disruption led to weaker wind speeds and variable directions, with both models capturing the general trends but exhibiting low correlations and notable biases, particularly UH-WRF’s overestimation by 0.46 m s^{-1} (Figure 15). The April 2023 cold frontal passage produced the strongest observed wind speeds (21.8 m s^{-1}); however, ERA5 significantly underestimated the peak (15.7 m s^{-1}) and missed an initial wind spike, while UH-WRF produced closer estimates (19.2 m s^{-1}) but with a 3-hour delay, highlighting issues in simulating mesoscale dynamics and turbulent mixing (Figure 16). The August 2023 event, influenced by Hurricane Dora’s circulation and stronger trade winds, resulted in rapid wind ramping, with ERA5 and UH-WRF capturing the overall trends but struggling with timing and magnitude (Figure 17). These events demonstrate the models’ strengths in representing general atmospheric patterns but also emphasize limitations in simulation finer-scale dynamics, boundary layer processes, and temporal variability during extreme weather conditions.~~To conclude our study and highlight the results in a wind energy context, we translate the wind speed errors for each simulation product to energy errors to assess what their impacts could be for an operating offshore wind farm. Following the form of Wagner et al. (2014), we calculate the rotor equivalent wind speeds for concurrent timestamps across the lidar observations, ERA5, and UH-WRF, assuming a hub height of 140 m. Applying the NREL 15 MW offshore wind reference power curve (Musial et al., 2019) to the lidar-based rotor equivalent wind speeds from the year-long Oahu deployment produces an estimated gross capacity factor of 59.8%. To explore the impacts of the wind speed biases noted for ERA5 (-1.53 m s^{-1} to -1.62 m s^{-1}) and UH-WRF (-0.24 m s^{-1} to -0.29 m s^{-1}) (Section 3.1) across the rotor layer, we apply the same power curve to the ERA5 and UH-WRF rotor equivalent wind speeds, which over the same time period results in estimated gross capacity factors of 42.2% and 56.0%, 18 and 4 percentage points lower than the estimate using the observations, respectively. On average over their respective temporal coverage periods, GWA3 and NOW-23 produce estimated capacity factors closer to the capacity factor based on observations than does ERA5: 52.7% (GWA3) and 63.5% (NOW-23) using the 15 MW reference power curve.~~

Onsite measurements spanning atmospheric layers ~~wind turbine rotor diameters~~ are critical to understanding the accuracy of the models and datasets used to characterize boundary layer dynamics through~~that drive the offshore wind industry through~~ resource assessment, wind trend analysis~~characterization~~, and downscaling. Studies like this one highlight the wealth of information that can be obtained for establishing observation-based ~~wind~~ characterizations of boundary layer processes, evaluating simulation accuracies, and ~~simulation correction possibilities and encourage further offshore wind observational campaigns in unstudied locations~~identifying opportunities for model correction. This work underscores the importance of conducting further observational campaigns in unstudied regions to improve understanding of boundary layer physics and strengthen model representations of atmospheric processes.

Appendix A: Summary of ~~Hawaii~~Hawai'i buoy observations and post-processing

A1 Instrumentation

Pacific Northwest National Laboratory (PNNL) operates lidar buoys that are owned by the U.S. Department of Energy to collect ~~offshore wind resource information in areas of potential commercial development~~atmospheric and oceanographic observations in under-studied regions. The buoys have previously collected measurements off the coast of Virginia, New Jersey, and California (Gorton and Shaw ~~et al.~~, 2020; Krishnamurthy et al, 2023). Prior to deployment off O'ahu, the lidar buoy underwent validation at Woods Hole Oceanographic Institution's Martha's Vineyard Coastal Observatory from January to June 2020 and was subsequently deployed off the Humboldt County, California coast from October 2020 to December 2021. The validation at Martha's Vineyard utilised an International Electrotechnical Commission-certified reference lidar atop an offshore platform approximately 250 m from the lidar buoy. The validation produced wind speed coefficients of determination (R^2) exceeding 0.98 and wind direction R^2 values exceeding 0.97 up to 200 m above sea level (a.s.l.) (Gorton and Shaw, 2020). The buoy~~y (Figure A1)~~ is equipped with a wind-profiling lidar capable of measuring wind speed up to 250 m above the instrument, surface meteorological measurements, oceanographic measurements, wave spectrum, and ocean current profile were collected from the instruments installed on the buoy~~ (Table A1)~~. A detailed discussion of the instrumentation aboard the buoy, which did not change between the California and Hawai'i deployments, is provided in Severy et al. (2021).

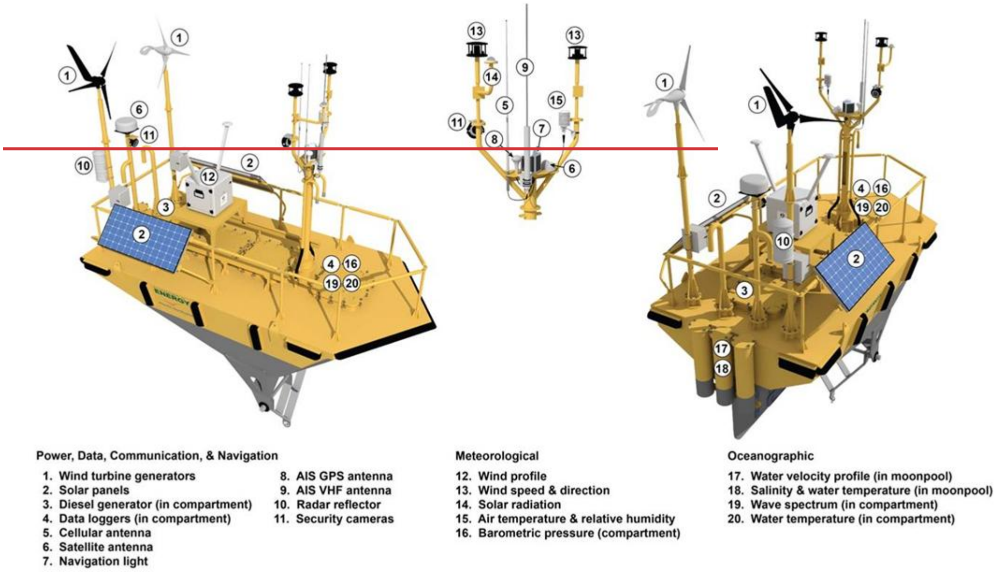

~~**Figure A1.** US Department of Energy Lidar Buoy schematic showing all meteorological and oceanographic observations.~~

~~**Table A1.** Sensor description.~~

~~**Reference Number**~~	~~**Sensor Type**~~	~~**Make/Model**~~	~~**Measurements**~~
~~12~~	~~Wind profiling lidar~~	~~Leosphere/Windcube 866~~	~~Vertical profile of wind speed and direction, wind dispersion, and spectral width~~
~~13~~	~~Ultrasonic anemometer (2)~~	~~Gill/WindSonic~~	~~2D wind velocity and direction, near surface~~
~~14~~	~~Pyranometer~~	~~Licor/LI-200~~	~~Global solar radiation~~
~~15~~	~~Temperature, relative humidity~~	~~Rotronic/MP101A~~	~~Air temperature, relative humidity~~
~~16~~	~~Barometer~~	~~RM Young/61302V~~	~~Atmospheric pressure~~
~~17~~	~~Acoustic Doppler current profiler (ADCP)~~	~~Nortek/Signature 250~~	~~Ocean velocity and direction from sea surface to 200 m water depth~~

~~**18**~~	~~Conductivity temperature depth (CTD)~~	~~Seabird/SBE 37SMP-1j-2-3c~~	~~Conductivity, sea surface temperature~~
~~**19**~~	~~Directional wave sensor~~	~~AXYS/TRIAXYS NW II~~	~~Directional wave spectra, wave height, wave time period~~
~~**20**~~	~~Water temperature~~	~~AXYS /YSI~~	~~Sea surface temperature~~
~~**N/A**~~	~~Inertial measurement unit (underneath the Doppler lidar)~~	~~MicroStrain/3DM GX5 45~~	~~Yaw, pitch, roll, linear velocity, global position, magnetometer, gyroscope~~

A2 Field deployment summary

A 12-month measurement campaign of atmospheric and oceanographic conditions using an AXYS WindSentinel buoy was conducted off the eastern coast of ~~Oahu~~O’ahu, ~~Hawaii~~Hawai’i, (Figure A1~~2~~) from December 2022 through December 2023 (Table A1~~2~~). Instruments on the buoy were operational throughout the field campaign, with the exception of those mentioned below. After the initial deployment the wave sensor was observed to be not operational; a service visit was completed on 16 March 2023, at 1:20 pm (HST) to repair the sensor. In addition, the lowest measurement height (40 m) of the Doppler lidar was adjusted to 50 m on 28 April 2023 due to the anomalous behaviour that was observed at 40 m range-gate. Post-deployment a thorough servicing of the lidar unit was conducted by the manufacturer, and it was determined that only the measurements from 40 m to 49 m were impacted due to an issue with the lidar’s master oscillator power amplifier. Therefore, we recommend that data only above 50 m be used for any future analysis. Later in the spring of 2023, the air temperature sensor was producing occasional faulty measurements; once the weather allowed, a second service visit was completed to replace the air temperature and relative humidity sensor on 5 September 2023, at 10:00 am (HST). On 14 December 2023, 14:00 (HST), the sensors were powered down to conserve energy after receiving a low fuel warning. The wave sensor and surface wind anemometer along with the safety and navigation equipment remained powered on to track the buoy location and monitor weather conditions to find a suitable recovery window. On 15 January 2024, at 8:30 am (HST), the buoy mooring was recovered, and the buoy was towed back to shore.

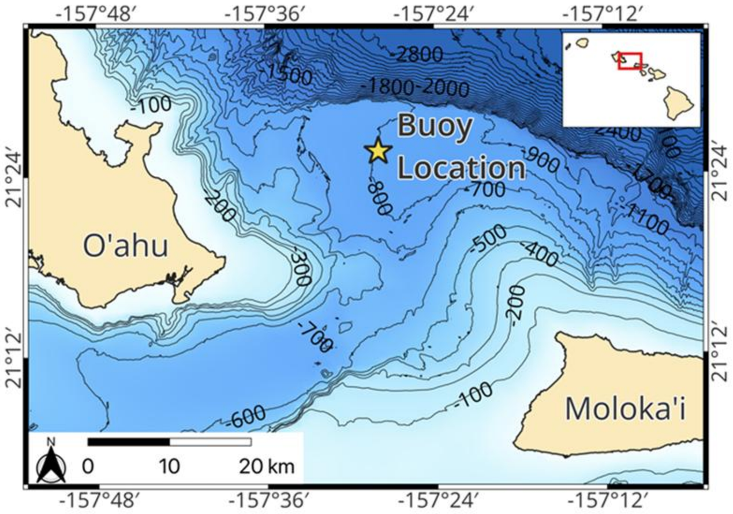

Figure A1~~2~~. Buoy deployment location.

Table A1~~2~~. Deployment parameters.

Deployment location	21.42605°N, 157.46678°W
Water depth	Approximately 815 m
Mooring exclusion radius	894 m
Deployment start date	1 December 2022 13:20 (HST)
Service visit #1	16 March 2023 13:20 (HST)
Service visit #2	5 September 2023 10:00 (HST)
Sensors powered down	14 December 2023 14:00 (HST)
Deployment recovery	15 January 2024 08:30 (HST)

A3 Data quality control

Throughout the field campaign, measurements collected from the buoy were transmitted via satellite communication to the DOE Wind Data Hub (http://a2e.energy.gov/project/buoy/data). Measurements from the wind profiling lidar are contained in buoy/lidar.z07.* files; measurements from the other instruments are contained in the buoy/buoy.z07.* files; images from the onboard cameras are contained in the buoy/camera.z07.00 files. Datasets appended with *.00 are for raw data; datasets appended with *.a0 are for data processed based on automated quality control scripts. This section described the production of the *.b0 dataset, which performs a quality control on the measurements based on post-processing and evaluation of instrument function and realistic physical phenomena. The data quality control for this field campaign was very similar to previous buoy deployments, details provided in Krishnamurthy et al., 2023.

A3.1 Surface meteorology on the buoy

Each surface meteorological measurement (wind speed, wind direction, air pressure, air temperature, and relative humidity) was subjected to the quality control methodology of Krishnamurthy et al. (2023). At each 10-minute timestamp, the surface measurements were evaluated and determined to be of good quality, missing (due to a power outage, communication issue, or instrument availability issue), or suspect or incorrect based on typical and physical expectations (Figure A2~~3~~).

During the ~~Hawaii~~Hawai'i deployment, 5% of the surface measurements (all variables) were missing due to communication issues. At no time periods were the surface measurements deemed suspect or missing due to a buoy power outage. The portside and starboard wind speeds, portside and starboard wind directions, relative humidity, and pressure were missing due to instrument availability for less than 2% of the deployment. No instances of incorrect data were noted for the portside and starboard wind speeds, portside and starboard wind directions, and pressure, and only three instances of incorrect data (0.01%) were determined for the relative humidity, leaving 93% - 94% of good data availability for these surface variables (Figure A2~~3~~).

Between 13 March 2023 and 6 September 2023, much of the air temperature data were deemed unphysical, with reported temperatures ranging between -36°C and 60°C. Due to this data quality issue, 42% of the air temperature measurements gathered during the ~~Hawaii~~Hawai'i deployment were classified as incorrect. An additional 5% of the air temperature measurements were missing due to instrument availability, leaving 47% of the data designated with good quality and availability (Figure A2~~3~~).

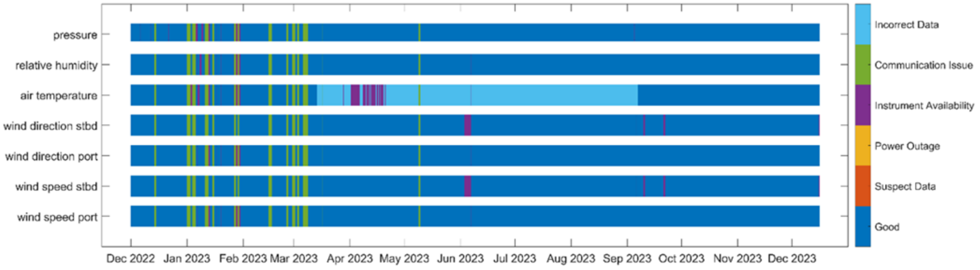

Figure A2~~3~~. Surface meteorological data availability and quality.

In terms of capturing the temporal variability of the near surface wind speeds, the port and starboard wind speed instruments aboard the buoys were in near-perfect agreement during the ~~Hawaii~~Hawai'i deployment, with a Pearson's correlation coefficient of 0.9993. However, a small bias (0.05 m s^{-1}) exists between the two instruments during the period of overlapping data availability, with the port wind speed measurements being slightly faster. Similarly, the portside wind directions are on average 3° greater than the starboard wind directions.

A3.2 Buoy Doppler lidar

Height-resolved measurements of wind speed, wind direction, and turbulent intensity were provided by a Windcube v2 Doppler lidar~~, as shown in Figure A1~~. This buoy and lidar had previously been deployed off the California coast near Humboldt Bay. For the ~~Hawaii~~Hawai'i deployment, the Windcube was initially configured in the same manner, with 12 measurement heights ranging every 20 m from 40 to 240 m (Krishnamurthy et al., 2023). The lowest measurement height was adjusted up to 49 m on 28 April 2023 due to suspected bias in the results at 40 m AGL, as mentioned previously. The heights of the other 11 measurement heights remained unchanged throughout the deployment.

The raw 1-Hz wind profiles measured by the Windcube were corrected for platform motion. For the current deployment, we use the same motion-correction procedure that was applied during a previous deployment near Humboldt Bay, California (Krishnamurthy et al., 2023). This procedure uses input from an externally mounted backup inertial measurement unit (IMU) to essentially bypass the lidar's internal IMU which had malfunctioned. Further details about the motion-correction process are provided by Krishnamurthy et al. (2023).

Motion-corrected 1-Hz data are used to compute ten-minute averages of wind speed, wind speed variance, wind direction, wind direction variance, as well as velocity variances and covariances. Prior to averaging, the 1-Hz data were filtered to remove poor quality samples with carrier-to-noise-ratios (CNR) below –23 dB. Velocity variances were computed by first linearly detrending the 1-Hz data (Krishnamurthy et al., 2023). The data availability was also computed as the percentage of 1-second samples above the CNR threshold (-23 dB). We note, however, that there was a small amount of deadtime associated with the IMU data. Raw 10-Hz IMU were stored in half-hourly files, which were not temporally contiguous. There was about a 30-second gap at the beginning and end of each raw IMU file. This resulted in a 1-minute gap every 30-minutes. As a result, the data availability is ultimately limited by these short gaps in the raw IMU data.

Figure A~~3~~4 shows the profile of lidar data availability (DA) during the ~~Hawaii~~Hawai'i deployment. The data availability represents the percentage of time that valid 1-Hz measurements are available within each 10-minute averaging period. It is important to note that the DA is computed over the time for which valid data exist. As a result, the DA for the two lowest measurement heights were computed over shorter time periods than the other heights. The data availability generally degrades with altitude, particularly above about 150 m AGL. The height-averaged DAs was 98%. As noted above, the DA is ultimately limited by the dead time in the raw 10Hz IMU data.

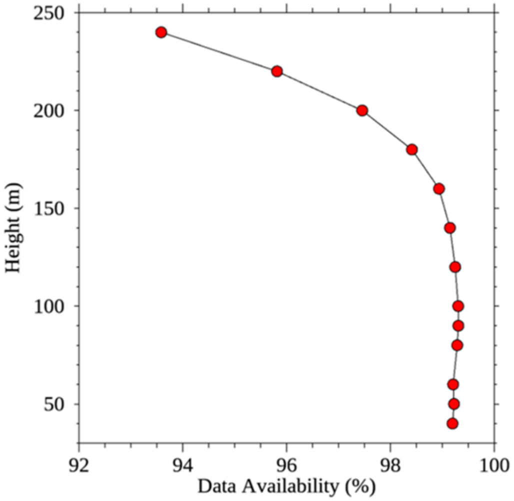

Figure A34. Data availability for the lidar winds during the ~~Hawaii~~Hawai'i deployment. The data availability for the lowest measurement height (40 m) was computed over the period from 1 December 2022 to 28 April 2023, post which the measurement at this height was not recorded anymore due to an issue observed at this height. The data availability at 50 m was computed over the period from 29 April to 14 December 2023. The data availability at 60 m and above was computed over the period from 1 December 2022 to 14 December 2023.

The wind speed profiles shown in Figure A4~~5~~a exhibit very little shear above the 50 m. At 100 m AGL the median wind speeds range from about 8.5 to 9.5 m s^{-1}, depending on the averaging period. This is significantly smaller than the wind resources observed by this same lidar off the California coast (Krishnamurthy et al., 2023). Also shown in Figure A4~~5~~a are profiles of the median wind speed during periods with positive and negative air-sea temperature differences. Here the air-sea temperature is used to indicate stable versus unstable conditions. The air-sea temperature difference was obtained from difference between air temperature sensor at ~3 m, and the CTD water temperature sensor at a water depth of ~1 m. We found that the air-sea temperature differences to be negative (unstable) 64% of the time during the deployment period.

Shown in Figure A4~~5~~c are profiles of the difference between the motion-corrected and uncorrected wind speed and wind direction. The wind speed differences are quite small, with the motion-corrected wind speeds only about 2 mm s^{-1} faster than the uncorrected winds. By contrast, motion-correction had a significant effect on the wind direction, as one would expect. The lidar wind direction profiles shown in Figure A4~~5~~ indicate a strong preference for easterly flow, and no significant rotation with height within the first 250 m above the sea surface.

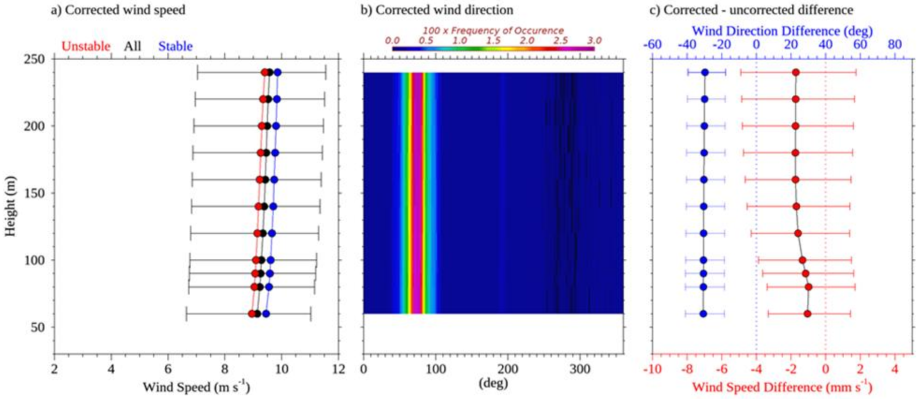

Figure A4~~5~~. Results from the Windcube v2 averaged from 29 April 2023 to 14 December 2023 showing (a) the median corrected wind speed profile (black), b) the corrected wind direction distribution profile, and (c) the difference between the motion-corrected and uncorrected wind speed and wind direction. Also shown in (a) are the median wind speed profiles for periods with positive (blue) and negative (red) air-sea temperature differences. Error bars show the 25th to 75th percentile range.

A3.3 Buoy oceanographic measurements

Surface gravity wave (i.e., wave) data were measured with the TRIAXYS sensor at a 20-minute sampling interval, the typical standard for wave measurements in the United States (NDBC, 1996). Wave measurements began on 16 March 2023, following the first service visit and ended with the deployment recovery on 15 January 2024. Initial quality control checks (i.e., included in *.a0 files on the Wind Data Hub) follow AXYS specifications and remove erroneous data by comparing individual measurements to temporally adjacent ones and removing all data when significant wave height reads larger than 40 m (AXYS, 2012). All data measured by the TRIAXYS wave sensor are given in Table A3. The mean wave period is calculated from the zeroth and first spectral moments of the wave spectra, differing from average wave period, T_{avg}, which is a mean of the time series. Peak wave period and peak wave direction are also calculated from the wave spectrum and not directly measured. AXYS post-processing software (version 5.01) is used to calculate the wave spectrum, which applies the maximum entropy method (Nwogu, 1989).

A nearby National Data Buoy Center (NDBC) buoy (#51202: Mokapu Point) was used to cross-check the lidar buoy wave measurements. Station 51202 is 21 km from and ~700 m shallower (depth = 86 m) than the ~~Oahu~~O'ahu lidar buoy location. The shallower depth allows some wave frequencies to transition from deep-water (i.e., $D > L/2$, where D is depth and L is wavelength) to transitional waves (i.e., $L/20 < D < L/2$). A comparison of significant wave heights between locations outlines largely similar wave climates, though the lidar buoy recorded wave heights slightly larger offshore than at 51202 (Figure A5~~6~~). Multiple factors could create this variability: deep water – transitional wave transformation, as well as variability in local bathymetry and wind fields; highlighting the importance of local measurements for wave applications. The minimum significant wave height measured at 51202 for the deployment period was 0.6 m, so significant waves heights less than 0.25 m at the lidar buoy were flagged as bad. If significant wave heights were marked bad for exceeding 40 m or failing to surpass 0.25 m, the remaining variables were also marked bad, as they are derived from the same sensor.

An additional quality check was applied to identify possible rogue waves. A ratio of maximum wave height to significant wave height (H_{max}/H_{sig}) greater than 2 is typically considered indicative of a rogue wave (e.g., Müller et al., 2005; Nikolkina & Didenkulova, 2011). Data points where rogue waves are possible would be marked as questionable, but we found no data in this deployment to exceed that criterion. Table A3 outlines the total number of good, questionable, and bad data for each measurement during the 16 March 2023, to 15 January 2024, wave sampling period. Other gaps in the wave and ocean observations were potentially due to a sensor failure and were not post-processed.

Table A3: TRIAXYS wave sensor measurements and number data marked good, questionable, or bad. Variables short names are provided to match those in *.b0 files, if applicable.

Wave measurement	**Good**	**Questionable**	**Bad**
Number zero crossings, ZCN	21,823	0	16
Average wave height, H_{avg}	21,817	0	22
Average wave period, T_{avg}	21,817	0	22
Maximum wave height, H_{max}	21,815	0	24
10th percentile wave height, H_{10}	21,817	0	22
10th percentile wave period, T_{10}	21,817	0	22
Significant wave height, H_{sig}	21,823	0	16
Significant wave period, T_{sig}	21,817	0	22
Mean wave direction	21,817	0	22
Mean wave spread	21,817	0	22
Mean wave period	21,817	0	22
Peak wave direction	0	0	21,839
Peak wave period	21,817	0	22

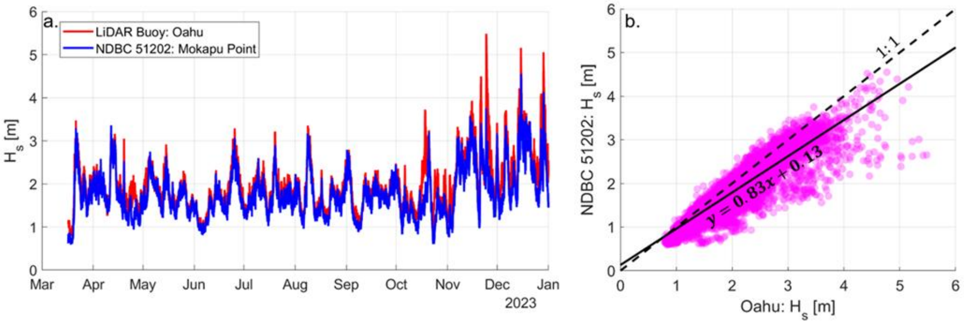

Figure A5~~6~~: (a) Significant wave heights measured at the lidar buoy (red) and NDBC station 51202 (blue) from 16 March 2023 to 31 December 2023. (b) Scatter comparison of significant wave heights from each station at each time step. A linear regression best fit is also shown.

Ocean currents were measured with the Nortek Signature 250 acoustic doppler current profiler (ADCP) using 10-minute ensemble averaging. The ADCP recorded measurements from the deployment start on 1 December 2022, through sensor power-down on 14 December 2023. Specifically, velocity magnitude and direction were measured at 50 depth bins, vertically spaced 4 m apart. Current magnitudes and direction were marked bad if: data was missing, spikes in current magnitude occurred that were spatially and temporally uncorrelated over a 10 min. duration, and/or a measurement was isolated in time (i.e., at least two successful measurements before and after did not occur). Current data were marked questionable if vertical shear in current speed was larger than 0.2 m s^{-1} and/or a vertical measurement was isolated in space (i.e., at least two successful measurements above and below did not occur). The ADCP sampling range typically reached 100 to 120 m in depth, with the deepest measurements at 141 m. Measurements below the sampling range are considered missing data and therefore marked as bad. In total, 999,158 current measurements were marked good, 80,261 were marked questionable, and 1,511,731 were marked bad.

Conductivity was measured with the Sea-Bird CTD and sea surface temperature (SST) from both the Sea-Bird CTD and YSI thermistor every 10 minutes over the same duration as the ADCP (1 December 2022 to 14 December 2023). CTD data were marked bad for either instrument if a spike in either SST or conductivity occurred which was temporally uncorrelated to surrounding data points. No “questionable” checks were applied to the CTD measurements. In total, the Sea-Bird CTD recorded 22,018 good and 29,805 bad conductivity and SST measurements. The YSI thermistor recorded 44,305 good and 7,518 bad SST measurements.

A3.4 Buoy pyranometer

In Krishnamurthy et al.~~,~~ (2023), we discussed the acquiring of coastal cloud properties obtained from broadband global solar radiation (GSR) data using the pyranometers (PYRs) deployed on the buoy. The difference between the measured surface irradiance and its estimated clear-sky counterpart (Figure A6~~7~~a) serves as the foundation for determining cloud optical thickness (COT, Figure A6~~7~~b) and generating the corresponding cloud mask (Figure A6~~7~~c). The COT characterizes the total reduction of downwelling solar radiation due to cloud droplets and/or ice crystals, and a dense cloud with a significant COT has a visually "dark" appearance to an observer on the surface. Thus, a large difference between the measured and clear-sky irradiances typically indicates the presence of a dense cloud above a pyranometer. Conversely, small differences suggest the chance of optically thin clouds. It is noteworthy that small differences may also be attributed to dense aerosol plumes originated by various sources, such as the somewhat unique ~~Hawaiian~~Hawaiian feature of vog, or also by fogs. Generally, optical thickness values for both aerosol plumes and fogs remain below 4. Consequently, the calculated COT values exceeding 4 provide greater confidence of cloud presence above the pyranometer, while lower values suggest otherwise (Figure A6~~7~~b). In other words, the COT can be viewed as a form of quality assurance (QA) for assessing cloud properties, such as a binary cloud mask (Figure A6~~7~~c). We also perform supplementary QA checks to identify days where the PYR-measured GSR data exhibit incomplete daytime coverage, featuring extended gaps lasting up to several hours. Cloud properties are not provided for these identified days.

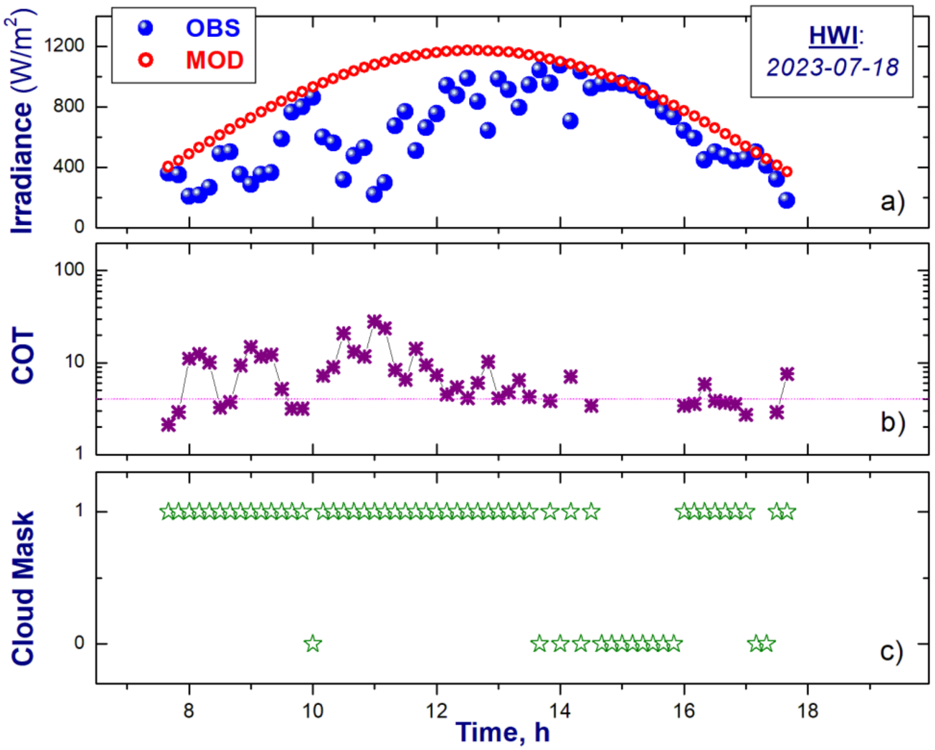

Figure A6~~7~~: (a) The GSR measured (OBS) for a given day (18 July 2023) and location (~~Hawaii~~Hawai'i) and its estimated (or model) clear-sky (MOD) counterpart; (b) calculated COT and (c) estimated cloud mask.

Data availability statement

The lidar buoy data utilized in this study are freely and publicly available from the U.S. Department of Energy. The ~~Hawaii~~Hawai'i lidar wind dataset is available at 10-minute and 1-Hz resolution at DOE (2025a) and DOE (2025c)~~https://doi.org/10.21947/2335446~~ and the accompanying near surface observations at DOE (2025b)~~https://doi.org/10.21947/2328673~~. ERA5 is provided via the Copernicus Climate Data Store at https://cds.climate.copernicus.eu/. UH-WRF was developed by the University of ~~Hawaii~~Hawai'i and shared with Pacific Northwest National Laboratory through a research partnership~~. NOW-23 is hosted by the National Renewable Energy~~

~~Laboratory's Wind Resource Database at https://wrdb.nrel.gov/data-viewer. Global Wind Atlas is available at https://globalwindatlas.info/en/.~~.

Author contributions

LS is responsible for conceptualization, data curation, formal analysis, and writing. RK provided conceptualization, supervision, and writing. RN, PS, and EK contributed data quality control and writing. TN, YC, FS, and NB developed some of the simulations used in this work and reviewed the manuscript. WG and YL supported with data access, processing, and manuscript review. MP and MS were critical to the success of the observational campaign that provided the measurements used in this work.

Competing interests

The authors have no competing interests to declare.

Acknowledgements

This work was authored by the Pacific Northwest National Laboratory, operated for the U.S. Department of Energy by Battelle (contract no. DE-AC05-76RL01830). This work was authored in part by the National Renewable Energy Laboratory for the U.S. Department of Energy (DOE) under Contract No. DE-AC36-08GO28308. Funding provided by U.S. Department of Energy Office of Energy Efficiency and Renewable Energy Wind Energy Technologies Office. The views expressed in the article do not necessarily represent the views of the DOE or the U.S. Government. The U.S. Government retains and the publisher, by accepting the article for publication, acknowledges that the U.S. Government retains a nonexclusive, paid-up, irrevocable, worldwide license to publish or reproduce the published form of this work, or allow others to do so, for U.S. Government purposes.

The authors would like to thank the U.S. Department of Energy Wind Energy Technologies Office for funding this research. PNNL would also like to thank the Wind Data Hub Team, especially Kenneth Burk, Max Levin, Chitra Sivaraman, Matthew McDuff, and Sherman Beus. The team would also like to acknowledge the buoy contractor, AXYS technologies, for their support maintaining the buoys and for data verification during the deployment and Raj Rai, Amy Brice, and James Marquis for reviewing the initial draft article.

References

Argüeso, D. and Businger, S.: Wind power characteristics off ~~Oahu~~O'ahu, ~~Hawaii~~Hawai'i, Renewable Energy, 128, 324-336, https://doi.org/10.1016/j.renene.2018.05.080, 2018.

AXYS Technologies Inc: TRIAXYSTM Directional Wave Buoy User's Manual, Version 12, Sydney, British Columbia, Canada, 2012.

Bianco, L., Mendeke, R., Lindblom, J., Djalalova, I. V., Turner, D. D., and Wilczak, J. M.: Evaluating the ability of the operational High Resolution Rapid Refresh model version 3 (HRRRv3) and version 4 (HRRRv4) to forecast wind ramp events in the US Great Plains, Wind Energy Science, 10, 2117-2136, https://doi.org/10.5194/wes-10-2117-2025, 2025.

Bodini, N., Optis, M., Redfern, S., Rosencrans, D., Rybchuk, A., Lundquist, J. K., Pronk, V., Castagneri, S., Purkayastha, A., Draxl, C., Krishnamurthy, R., Young, E., Roberts, B., Rosenlieb, E., and Musial, W.: The 2023 National Offshore Wind data set (NOW-23), Earth Syst. Sci. Data, 16, 1965–2006, https://doi.org/10.5194/essd-16-1965-2024, 2024a.

Bodini, N., Optis, M., Liu, M. Gaudet, B. Krishnamurthy, R., Kumler, A., Rosencrans, D., Rybchuk, A., Tai, S.-L., Berg, L., Musial, W., Lundquist, J. K., Purkayastha, A., Young, A., and Draxl, C.: Causes of and Solutions to Wind Speed Bias in NREL's 2020 Offshore Wind Resource Assessment for the California Pacific Outer Continental Shelf, National Renewable Energy Laboratory (NREL), Golden, Colorado, United States, NREL/TP-5000-88215, https://docs.nrel.gov/docs/fy24osti/88215.pdf, 2024b.

Bucci, L.: Hurricane Dora, National Hurricane Center Tropical Cyclone Report, EP052023, https://www.nhc.noaa.gov/data/tcr/EP052023_Dora.pdf, 5 March 2024.

Buster, G., Pinchuk, P. Lavin, L., Benton, B., and Bodini, N.: Bias Correcting NOAA's High-Resolution Rapid Refresh (HRRR) Wind Resource Data for Grid Integration Applications, https://docs.nrel.gov/docs/fy25osti/91749.pdf, 2024.

Carta, J. A., Velázquez, S., and Cabrera, P.: A review of measure-correlate-predict (MCP) methods used to estimate long-term wind characteristics at a target site, Renewable and Sustainable Energy Reviews, 27, 362-400, https://doi.org/10.1016/j.rser.2013.07.004, 2013.

CDS (Climate Data Store): Complete ERA5 global atmospheric reanalysis~~ERA5 hourly data on single levels from 1940 to present~~ [data set], https://cds.climate.copernicus.eu/datasets/reanalysis-era5-complete~~https://cds.climate.copernicus.eu/datasets/reanalysis-era5-single-levels~~, accessed 7 January 2025a.

CDS (Climate Data Store): ERA5 hourly data on single levels from 1940 to present [data set], https://cds.climate.copernicus.eu/datasets/reanalysis-era5-single-levels, accessed 26 November 2025b.

Cowin, E., Wang, C., and Walsh, S. D. C.: Assessing predictions of Australian Offshore Wind Energy Resources from Reanalysis Datasets, Energies, 16(8), 3404, https://doi.org/10.3390/en16083404, 2023.

Davis, N. N., Badger, J., Hahmann, A. N., Hansen, B. O., Mortensen, N. G., Kelly, M., Larsén, X. G., Olsen, B. T., Floors, 485 R., Lizcano, G., Casso, P., Lacave, O., Bosch, A., Bauwens, I., Knight, O. J., Potter van Loon, A., Fox, R., Parvanyan, T., Krohn Hansen, S. B., Heathfield, D., Onninen, M., and Drummond, R.: The Global Wind Atlas: A High-Resolution Dataset of Climatologies and Associated Web-Based Application, Bulletin of the American Meteorological Society, 104.8, E1507-E1525, https://doi.org/10.1175/BAMS-D-21-0075.1, 2023.

DOE (U.S. Department of Energy): 10 min Lidar Winds/Derived Data [data set], https://wdh.energy.gov/ds/buoy/lidar.z07.c0~~https://a2e.energy.gov/ds/buoy/lidar.z07.c0~~, accessed 6 January 2025a.

DOE (U.S. Department of Energy): Hawai'i - Wind Sentinel (120), Oahu, Hawai'i / Reviewed Data [data set], https://wdh.energy.gov/ds/buoy/buoy.z07.b0, accessed 6 January 2025b.

DOE (U.S. Department of Energy): 1Hz Lidar Winds / Reviewed Data [data set], https://wdh.energy.gov/ds/buoy/lidar.z07.b0, accessed 24 November 2025c.

DTU (Technological University of Denmark): Global Wind Atlas [data set], https://globalwindatlas.info/en, accessed 7 January 2025.

Edson, J. B., Jampana, V., Weller, R. A., Bigorre, S. P., Plueddemann, A. J., Fairall, C. W., Miller, S. D., Mahrt, L., Vickers, D., and Hersbach, H.: On the Exchange of Momentum over the Open Ocean, Journal of Physical Oceanography, 43, 8, 1589-1610, https://doi.org/10.1175/JPO-D-12-0173.1, 2013.

Fragano, C. G. and Colle, B. A.: Validation of Offshore Winds in the ERA5 Reanalysis and NREL NOW-23 WRF Analysis Using Two Floating Lidars in the New York Bight, Weather and Forecasting, 1307-1323, https://doi.org/10.1175/WAF-D-24-0155.1, 2025.

Gandoin, R. and Garza, J.: Underestimation of strong wind speeds offshore in ERA5: evidence, discussion and correction, Wind Energy Science, 9, 1727-1745, https://doi.org/10.5194/wes-9-1727-2024, 2024.

Gaudet, B. J., García Medina, G., Krishnamurthy, R., Shaw, W. J., Sheridan, L. M., Yang, Z., Newsom, R. K., and Pekour, M.: Evaluation of Coupled Wind–Wave Model Simulations of Offshore Winds in the Mid-Atlantic Bight Using Lidar-Equipped Buoys, Monthly Weather Review, 150, 1377-1395, https://doi.org/10.1175/MWR-D-21-0166.1, 2022.

Gaudet, B. J., García Medina, G., Krishnamurthy, R., Sheridan, L. M., Yang, Z., Newsom, R. K., Pekour, M., Gustafson Jr., W. I., and Liu, J.: Assessing Impacts of Waves on Hub-Height Winds off the U.S. West Coast Using Lidar Buoys and Coupled Modeling Approaches, Pacific Northwest National Laboratory, Richland, WA, United States, PNNL-35856, https://doi.org/10.2172/2337529, 2024.

Gelaro, R., McCarty, W., Suárez, M. J., Todling, R., Molod, A., Takacs, L., Randles, C. A., Darmenov, A., Bosilovich, M. G., Reichle, R., Wargan, K., Coy, L., Cullather, R., Draper, C., Akella, S., Buchard, V., Conaty, A., da Silva, A. M., Gu, W., Kim, G-K., Koster, R., Lucchesi, R., Merkova, D., Nielsen, J. E., Partyka, G., Pawson, S., Putnam, W., Rienecker, M., Schubert, S. D., Sienkiewicz, M., and Zhao, B.: The Modern-Era Retrospective Analysis for Research and Applications, Version 2 (MERRA-2), J. Climate, 30, 5419–5454, https://doi.org/10.1175/JCLI-D-16-0758.1, 2017.

Gorton, A. M. and Shaw, W. J.: Advancing offshore wind resource characterization using buoy-based observations, Mar. Technol. Soc. J., 54, 37-43, https://doi.org/10.4031/MTSJ.54.6.5, 2020.

Hansen, K. S., Barthelmie, R. J., Jensen, L. E., Sommer, A.: The impact of turbulence intensity and atmospheric stability on power deficits due to wind turbine wakes at Horns Rev wind farm, Wind Energy, 15(1), 183-196, https://doi.org/10.1002/we.512, 2011.

Hayes, L., Stocks, M., and Blakers, A.: Accurate long-term power generation model for offshore wind farms in Europe using ERA5 reanalysis, Energy, 229, 120603, https://doi.org/10.1016/j.energy.2021.120603, 2021.

Hersbach, H., Bell, B., Berrisford, P., Hirahara, S., Horányi, A., Muñoz-Sabater, J., Nicolas, J., Peubey, C., Radu, R., Schepers, D., Simmons, A., Soci, C., Abdalla, S., Abellan, X., Balsamo, G., Bechtold, P., Biavati, G., Bidlot, J., Bonavita, M., De Chiara, G., Dahlgren, P., Dee, D., Diamantakis, M., Dragani, R., Flemming, J., Forbes, R., Fuentes, M., Geer, A., Haimberger, L., Healy, S., Hogan, R. J., Hólm, E., Janisková, M., Keeley, S., Laloyaux, P., Lopez, P., Lupu, C., Radnoti, G., de Rosnay, P., Rozum, I., Vamborg, F., Villaume, S., and Thépaut, J.-N.: The ERA5 Global Reanalysis, Q. J. Roy. Meteor. Soc., 146, 1999–2049, https://doi.org/10.1002/qj.3803, 2020.

Hsiao, F., Chen, Y.-L., and Hitzl, D. E.: Heavy rainfall events over central ~~Oahu~~O’ahu under weak wind conditions during seasonal transitions, Monthly Weather Review, 148, 4117-4141~~-~~, https://doi.org/10.1175/MWR-D-19-0358.1, 2020.

Hsiao, F., Chen, Y.-L., Nguyen, H. P., Hitzl, D. E., and Ballard, R.: Effects of Trade Wind Strength on Airflow and Cloudiness over ~~Oahu~~O'ahu, Monthly Weather Review, 149 (9), 3037-3062, https://doi.org/10.1175/MWR-D-20-0399.1, 2021.

Jimenez, T., Keyser, D., and Tegen, S.: Floating Offshore Wind in ~~Hawaii~~Hawai'i: Potential for Jobs and Economic Impact from Two Future Scenarios, National Renewable Energy Laboratory, Golden, CO, United States, NREL/TP-5000-65481, https://www.nrel.gov/docs/fy16osti/65481.pdf, 2016.

Kalverla, P. C., Duncan Jr., J. B., Steeneveld, G.-J., and Holtslag, A. A. M.: Low-level jets over the North Sea based on ERA5 and observations: together they do better, Wind Energy Science, 4, 193-209, https://doi.org/10.5194/wes-4-193-2019, 2019.

Kalverla, P. C., Holtslag, A. A. M., Ronda, R. J., and Steeneveld, G-J.: Quality of wind characteristics in recent wind atlases over the North Sea, Quarterly Journal of the Royal Meteorological Society, 146(728), 1498-1515, https://doi.org/10.1002/qj.3748, 2020.

Krishnamurthy, R., García Medina, G., Gaudet, B., Gustafson Jr., W. I., Kassianov, E. I., Liu, J., Newsom, R. K., Sheridan, L. M., and Mahon, A. M.: Year-long buoy-based observations of the air–sea transition zone off the US west coast, Earth Syst. Sci. Data, 15, 5667–5699, https://doi.org/10.5194/essd-15-5667-2023, 2023.

Lee, J., Ghate, V. P., Mitra, A., Miller, L. M., Krishnamurthy, R., and Egerer, U.: Characterization of HRRR-simulated rotor layer wind speeds and clouds along the coast of California, Wind Energy Science, 10(11), 2755-2769, https://doi.org/10.5194/wes-10-2755-2025, 2025.

Longman, R. J., Elison Timm, O., Giambelluca, T. W., and Kaiser, L.: A 20-Year Analysis of Disturbance-Driven Rainfall on O'ahu, Hawai'i, Monthly Weather Review, 149, 6, 1767-1783, https://doi.org/10.1175/MWR-D-20-0287.1, 2021.

Lu, B-Y., Chu, P-S., Kim, S-H., and Karamperidou, C.: Hawaiian Regional Climate Variability during Two Types of El Niño, Journal of Climate, 33, 22, 9929-9943, https://doi.org/10.1175/JCLI-D-19-0985.1, 2020.

Mass, C. and Ovens, D.: The Meteorology of the August 2023 Maui Wildfire, Weather and Forecasting, 39(8), 1097-1115, https://doi.org/10.1175/WAF-D-23-0210.1, 2024.

McCoy, A., Musial, W., Hammond, R., Mulas Hernando, D., Duffy, P., Beiter, P., Pérez, P., Baranowski, R., Reber, G., and Spitsen, P.: Offshore Wind Market Report: 2024 Edition, National Renewable Energy Laboratory, Golden, CO, United States, NREL/TP-5000-90525, https://www.nrel.gov/docs/fy24osti/90525.pdf, 2024.

Morrison, I. and Businger, S.: Synoptic Structure and Evolution of a Kona Low, Weather and Forecasting, 16, 81-98, https://doi.org/10.1175/1520-0434(2001)016%3C0081:SSAEOA%3E2.0.CO;2, 2001.

Müller, P., Garrett, C., and Osborne, A.: Rogue waves, Oceanogr., 18, 3, 66-75, https://doi.org/10.5670/oceanog.2005.30, 2005.

Musial, W., Beiter, P., Nunemaker, J., Heimiller, D., Ahmann, J., and Busch, J.: Oregon Offshore Wind Site Feasibility and Cost Study, National Renewable Energy Laboratory, Golden, CO, United States, NREL/TP-5000-74597, https://doi.org/10.2172/1570430, 2019.

NASA (National Aeronautical and Space Administration~~NASA (National Aeronautical and Space Administration~~): MERRA-2 inst1_2d_asm_Nx: 2d, 1-Hourly, Instantaneous, Single-Level, Assimilation, Single-Level Diagnostics V5.12.4 (M2I1NXASM) [data set], https://disc.gsfc.nasa.gov/datasets/M2I1NXASM_5.12.4/summary, accessed 7 January 2025.

NDBC (National Data Buoy Center~~ (NDBC~~): Nondirectional and Directional Wave Data Analysis Procedures, NDBC Technical Document 96-01, Stennis Space Center, Slidell, Louisiana, USA, https://www. ndbc.noaa.gov/wavemeas.pdf, ~~(~~last access: 12 March 2024~~)~~, 1996.

NOAA (National Oceanic and Atmospheric Administration): Kona Lows Produce Two Rounds of Flooding - February 2023, https://www.weather.gov/hfo/KonaLowFeb2023, last access: 18 November 2025, 2023a.

NOAA (National Oceanic and Atmospheric Administration): Cold Front Brings Winds and Rain to Hawai'i - April 2023, https://www.weather.gov/hfo/coldfront_apr2023, last access: 18 November 2025, 2023b.

NOAA (National Oceanic and Atmospheric Administration): Climate Variability: Oceanic Niño Index, https://www.climate.gov/news-features/understanding-climate/climate-variability-oceanic-nino-index, last updated 25 June 2025.

NREL (National Renewable Energy Laboratory~~NREL~~): Wind Resource Database [data set], https://wrdb.nrel.gov/data-viewer, accessed 7 January 2025.

Nehzad, M., Neshat, M., Groppi, D., Marzialetti, P., Heydari, A., Sylaios, G., and Astiaso Garcia, D.: A primary offshore wind farm site assessment using reanalysis data: a case study for Samothraki island, Renew. Energ., 172, 667–679, https://doi.org/10.1016/j.renene.2021.03.045, 2021.

Nikolkina, I. and Didenkulova, I.: Rogue waves in 2006-2010, Nat. Hazards Earth Syst. Sci., 11, 2913–2924, https://doi.org/10.5194/nhess-11-2913-2011, 2011.

~~NREL: Wind Resource Database [data set], https://wrdb.nrel.gov/data-viewer, accessed 7 January 2025.~~

~~Nunalee, C. G. and Basu, S.: Mesoscale modeling of coastal low-level jets: implications for offshore wind resource estimation, Wind Energy, 17, 1199–1216, https://doi.org/10.1002/we.1628, 2014.~~

Nwogu, O.: Maximum entropy estimation of directional wave spectra from an array of wave probes, Appl. Ocean Res., 11, 176–182, 1989.

Pronk, V., Bodini, N., Optis, M., Lundquist, J. K., Moriarty, P., Draxl, C., Purkayastha, A., and Young, E.: Can reanalysis products outperform mesoscale numerical weather prediction models in modeling the wind resource in simple terrain?, Wind Energ. Sci., 7, 487–504, https://doi.org/10.5194/wes-7-487-2022, 2022.

Ramon, J., Lledó, L., Torralba, V., Soret, A., and Doblas-Reyes, F. J.: Which global reanalysis best represents near-surface winds?, Q. J. Roy. Meteor. Soc., 145, 3236–3251, https://doi.org/10.1002/qj.3616, 2019.

Severy, M., Gorton, A. M., Krishnamurthy, R., and Levin, M. S.: Lidar Buoy Data Dictionary: For the 2020 – 2021 California Deployments, Pacific Northwest National Laboratory (PNNL), Richland, WA, USA, PNNL-30947, https://doi.org/10.2172/1987710, 2021.

Sheridan, L. M., Krishnamurthy, R., Gorton, A. M., Shaw, W. J., and Newsom, R. K.: Validation of Reanalysis-Based Offshore Wind Resource Characterization Using Lidar Buoy Observation, Mar. Technol. Soc. J., 54, 44–61, https://doi.org/10.4031/MTSJ.54.6.13, 2020.

Sheridan, L. M., Krishnamurthy, R., García Medina, G., Gaudet, B. J., Gustafson Jr., W. I., Mahon, A. M., Shaw, W. J., Newsom, R. K., Pekour, M., and Yang, Z.: Offshore reanalysis wind speed assessment across the wind turbine rotor layer off the United States Pacific coast, Wind Energy Science, 7, 2059-2084, https://doi.org/10.5194/wes-7-2059-2022, 2022.

Sheridan, L. M., Krishnamurthy, R., Gustafson Jr., W. I., Liu, Y., Gaudet, B. J., Bodini, N., Newsom, R. K., and Pekour, M.: Offshore low-level jet observations and model representation using lidar buoy data off the California coast, Wind Energy Science, 9, 741-758, https://doi.org/10.5194/wes-9-741-2024, 2024.

Soares, P. M. M., Lima, D. C. A., and Nogueira, M.: Global offshore wind energy resources using the new ERA-5 reanalysis, Environ. Res. Lett., 15, 1040a2, 10.1088/1748-9326/abb10d, 2020.

Soukissian, T. H., Karathanaski, F. E., and Zaragkas, D. K.: Exploiting offshore wind and solar resources in the Mediterranean using ERA5 reanalysis data, Energy Conversion and Management, 237, 114092, https://doi.org/10.1016/j.enconman.2021.114092, 2021.

~~U.S. Energy Information Administration (EIA): Hawaii State Profile and Energy Estimates, https://www.eia.gov/state/?sid=HI, 18 April 2024.~~

Wagner, R., Cañadillas, B., Clifton, A., Feeney, S., Nygaard, N., Poodt, M., St. Martin, C. Tüxen, E., and Wagenaar, J. W.: Rotor equivalent wind speed for power curve measurement – comparative exercise for IEA Wind Annex 32, J. Phys.: Conf. Ser., 524, 012108, https://doi.org/10.1088/1742-6596/524/1/012108, 2014.

Wharton, S. and Lundquist, J. K.: Atmospheric stability affects wind turbine power collection, Environ. Res. Lett., 7, 014005, https://doi.org/10.1088/1748-9326/7/1/014005/meta, 2012.

Wilczak, J. M., Akish, E., Capotondi, A., and Compo, G. P.: Evaluation and bias correction of the ERA5 reanalysis over the United States for wind and solar energy applications, Energies, 17(7), 1667, https://doi.org/10.3390/en17071667, 2024.

Zhang, Y., Chen, Y.-L., Hong, S.-Y., Juang, H.-M. H., and Kodama, K.: Validation of the coupled NCEP Meso-scale Spectral Model and an advanced land surface model over the ~~Hawaiian~~Hawaiian Islands. Part I: Summer trade wind conditions and a heavy rainfall event. Wea. Forecasting, 20, 847-872, https://doi.org/10.1175/WAF891.1, 2005.